Enhancement of photocatalytic-based processes by mono- and bimetallic (CuPd) rutile loaded nanoparticles for antibiotic resistance genes and facultative pathogenic bacteria removal

Marta Gmurek [a,b,c,*], Johannes Alexander [c], Paweł Mazierski [d], Magdalena Miodyńska [d], Maciej Fronczak [a], Tomasz Klimczuk [e], Adriana Zaleska-Medynska [d], Harald Horn [b,f], Thomas Schwartz [c]

[a] Lodz University of Technology, Faculty of Process and Environmental Engineering, Department of Molecular Engineering, 90-924 Lodz, Poland
[b] Karlsruhe Institute of Technology, Engler-Bunte-Institut, Water Chemistry and Water Technology, 76131 Karlsruhe, Germany
[c] Karlsruhe Institute of Technology, Institute of Functional Interfaces, Microbiology/Molecular Biology Department, Eggenstein-Leopoldshafen, Germany
[d] University of Gdansk, Faculty of Chemistry, Department of Environmental Technology, 80-308 Gdańsk, Poland
[e] Gdansk University of Technology, Department of Solid State Physics, 80-233 Gdansk, Poland
[f] DVGW German Technical and Scientific Association for Gas and Water Research Laboratories, Water Chemistry and Water Technology, 76131 Karlsruhe, Germany

ARTICLE INFO

ABSTRACT

The aim of the study was the strong reduction of facultative pathogenic bacteria (FPB), and clinically relevant antibiotic resistance genes (ARGs) from secondary effluent. To evaluate the ARGs removal efficiency comparative study of individual unit processes and combined AOPs has been performed. The present work investigated: i) removal of selected ARGs, namely bla_{TEM}, ermB, qnrS, tetM, five FPB as well as 16S rDNA and the integrase gene $intl$1 involved in horizontal gene transfer; ii) bacterial regrowth potential after treatment; (iii) the removal of the total genomic DNA content, by mono- and bimetallic TiO_2-CuPd rutile photocatalysts under visible light radiation in real secondary effluent. The nanoparticles were characterized by UV–vis, XRD, HRTEM, Raman and XPS. TiO_2-CuPd/VIS inactivation gives the highest (more than 2 log units removal) efficiency for almost all targets (bla_{TEM}, ermB, tetM, $intl$ 1, and 16S rRNA) compared to monometallic catalysts. The highest efficiency toward bla_{TEM} was achieved after ozonation and TiO_2-CuPd/O_3/VIS (3.22 and 3.23 LRV, respectively). It was found that despite similar FPB inactivation, lower DNA destruction was found after O_3 compared to TiO_2-CuPd/O_3/VIS treatment. The bla_{TEM} and enterococci were completely removed during TiO_2-CuPd/O_3/Vis and TiO_2-Cu/O_3/Vis. While, catalytic ozonation leads to only slightly bla_{TEM} removal (0.64 and 0.44 LRV for TiO_2-CuPd/O_3 and TiO_2-Cu/O_3, respectively). Photocatalytic ozonation with the application of TiO_2-CuPd leads to significant removal of FPB and ARGs due to synergistic effect between Pd and Cu, which leads to acceleration of ozone – catalysts reaction. Photocatalytic ozonation has the greatest potential giving promising possibilities for eliminating AMR.

1. Introduction

The increased antibiotics concentration in effluents of wastewater treatments plants (even up to 1 µg/L [1,2], due to extensive antibiotic usage in medicine and veterinary has led to the appearance of various antibiotic-resistant bacteria (ARB) and antibiotic resistance genes (ARGs) [3–6]. Some of the ARB, even those not pathogenic, have the ability to transfer their resistance genes to human pathogens, which pose a potentially great risk to human health [5–8]. Some facultative

pathogenic bacteria are crucial in escalating resistance spreading, known as 'ESKAPE' group (*Enterococcus faecium, Staphylococcus aureus, Klebsiella pneumoniae, Acinetobacter baumannii, Pseudomonas aeruginosa,* and *Enterobacter spp.*) [9]. Since the ESKAPE group has been classified by the WHO as a priority group for infection and carrier of ARGs, their elimination during wastewater treatment is demanded for the efficient removal of resistance.

ARGs can be found in intracellular and extracellular DNA (iDNA and eDNA), both contributing to the overall abundances of ARGs in

wastewater compartments [10,11]. In addition, ARGs are often located on mobile genetic elements (MGEs), which facilitate the dissemination among taxonomically unrelated species [12]. Hence, antibiotic-resistant and facultative pathogenic bacteria pose a growing threat to public health and should therefore not be released into the environment. As the last common barrier of the different emission sources, such as wastewater from hospitals, nursing homes, slaughterhouses, private households, etc., the sewage treatment plant is a suitable place to centrally minimise the spread of antibiotic resistance genes and facultative pathogenic bacteria into the environment. There are no general and overarching regulations for the reduction of these facultative pathogenic bacteria and clinically relevant antibiotic resistance genes by wastewater treatment plants and the individual processes as well as the mode of operation of existing wastewater treatment plants are often not optimised for the retention of these microbiological contaminants [13,14].

It is well known that under stressed conditions, pathogens can enter a Viable But Non-Culturable state (VBNC), in which, can remain alive for long time and maintain their potential for virulence [15].

Advanced Oxidation Processes, especially ozonation and photocatalytic processes, gain attention due to their high efficiency in micropollutant removal as well as possible light and reactive oxygen species interactions. TiO$_2$ due to several advantages (e.g. inexpensive, and photoresponsive) is the best known photocatalyst. However, TiO$_2$ have poor light utilization due to the broad bandgap and insufficient charge separation caused by the quick recombination of photogenerated charge carriers. To increase the photoactivity with visible light of TiO$_2$ (Eg^{anatase} 3.2 eV, Eg^{rutile} 3.0 eV for wavelengths in the range of 390–410 nm [16]) several methods have been developed. One of the most promising is modification with noble metals (efficient separation of photo-generated electron–hole pairs, which prolong the lifetime of excited electrons). Moreover, under visible-light irradiation TiO$_2$ is activated by the plasmonic properties of noble metals [17–20]. It has also been suggested that the antibacterial qualities of noble metals together with the high photocatalytic activity of modified TiO$_2$ should lead to a high inactivation efficiency. However, this strategy has only seldom resulted in increased activity under solar irradiation. Moreover, it was found that the rate-limiting reaction in environmental photocatalysis is the reduction of oxygen by photogenerated electrons [16,21,22]. The kinetics of oxygen reduction at the photocatalyst surface can be improved by depositing a cocatalyst that would catalyse the transfer of photogenerated electrons to oxygen molecules. Decreased recombination and improved charge separation would result from TiO$_2$ ability to transport photogenerated electrons to oxygen molecules more quickly and therefore it seems to be a very promising technique for increasing photodegradation rates of TiO$_2$ photocatalysis. It has already been established that Cu decorated rutile photocatalysts show rapid photogenerated electron transfers to Cu(II/I) sites, which is followed by increased oxygen reduction catalysis, associated with improved charge separation and higher photocatalytic degradation rates [16].

The fundamental cause of photocatalysis low efficiency is charge recombination [16,21,22]. Moreover, the reaction rate of ozone-resistant pollutants limits ozonation [23]. Photocatalytic ozonation overcomes these drawbacks. The synergism between ozonation and photocatalytic oxidation with the application of TiO$_2$-based catalysts is well known to increase the oxidation rate and mineralization and decrease toxicity during antibiotics decomposition [3,23–30]. The synergy between photocatalysis and ozone causes a generation of a significant amount of Reactive Oxygen Species (ROS), like O$_3$, O$_2^{\cdot-}$, ^{1}O$_2$, H$_2$O$_2$ and $^\cdot$OH but also holes (h +) [24–29], that are responsible for high efficiency toward pharmaceuticals and other organic micropollutants.

Photocatalytic processes have been proved to be the most efficient for ARGs removal [4]. However, neither UVC, UVA nor visible light photocatalysis is able to completely remove ARGs. Therefore, the photocatalytic ozonation process seems to be reasonable to enhance the efficiency due to increase its photocatalytic activity by accelerating ROS.

The use of an additional oxidant in combination with photocatalyst may increase the removal rate and prevent regrowth. The application of visible light or solar photocatalytic ozonation can be found as the most efficient and cost-effective tertiary treatment for secondary effluents.

Main goal of the study was the strong reduction of facultative pathogenic bacteria (FPB), and clinically relevant ARGs by catalytic-ozone based posttreatment of biologically treated wastewater. Herein, we report a new highly efficient rutile-based bimetallic catalyst. That could be achieved by deposition of Cu redox cocatalysts for oxygen reduction onto TiO$_2$ (in order to enhance the intrinsic light activity of TiO$_2$ [16,31,32]) and improvement of visible light absorption ability by Pd deposition. The latter forms a Schottky barrier between TiO$_2$-Pd interface and transfers trapped electrons into adsorbed oxygen more effectively than the bare TiO$_2$ surface [33,34]. To evaluate the ARGs removal efficiency a comparative study of the individual processes and combined AOPs has been performed. Therefore, the following photocatalytic based processes were applied, i) photocatalytic inactivation with the application of mono- and bimetallic TiO$_2$-CuPd rutile nanoparticles, ii) ozonation, iii) photolytic ozonation iv) catalytic and v) photocatalytic ozonation. Hence, for the first time the problem of inactivation of ARGs and FPB by several catalytic-ozone based processes with the application of visible light photoactive monometallic and bimetallic nanoparticles supported on rutile TiO$_2$ has been tracked.

This work provides an effective and alternative strategy for the ARGs inactivation via photocatalytic ozonation under real conditions. Moreover, an insight into the mechanism underlying the process is provided. Apart from the novelty regarding bimetallic TiO$_2$- CuPd photocatalytic ozonation, for which no data exist in the literature, the study sheds some light on the regrowth potential of the bacteria conveying ARGs after photocatalytic processes for which little is known. Although the photocatalytic ozonation process is widely applied for micropollutant degradation, previous studies constantly stress that more research is needed to determine the mechanism of its action [35]. Furthermore, despite the well-documented capacity of photocatalytic ozonation to remove contaminants of emerging concern, its application in Waste Water Treatment Plants (WWTPs) as an advanced tertiary treatment, is not systematically considered. Hence, targeting this key knowledge gap is relevant and timely. It is worth noting that the proved insusceptibility of various bacterial species indigenously present in real waste water to ozone may be overcome by the photocatalytic ozonation process. This may have practical implications in designing processes for tertiary treatment. From this point of view, the study of photocatalytic-based processes by mono- and bimetallic (Cu and/or Pd) rutile loaded nanoparticles provides new information and adds important new knowledge for further research.

2. Experimental part

2.1. Photocatalytic experiments

Photocatalytic inactivation experiments were carried out in semi-batch mode in a glass-made reactor (0.25 L – working volume 0.2 L) with magnetic stirring, provided with a gas inlet, a gas outlet and a liquid sampling port. The reactor was placed in a solar simulator (Oriel Sol3A™ ClassAAA Solar Simulator, Newport Corp., Irvine, CA) equipped with a xenon arc lamp (1000 W, UV-cut off, visible light from 350 nm – 800 nm). The photon flux was measured as 448 W/m^2 by Oceans Optics USB 4000 fiber optic spectrometer.

The experiments were conducted at the inherent solution pH, with the catalyst dose of 200 mg/L for 2 h under air-equilibrated conditions (photocatalytic inactivation). Photocatalytic ozonation were conducted with the same catalysts dose. Additional ozone-based treatment was performed to investigate possible mechanism of inactivation. In order to investigate the effect of ozone-based technologies on the removal of ARGs and FPB in WWTP effluent, additional bench-scale ozonation experiments in semi-batch were conducted. An ozone generator (BMT 803

BT, BMT Messtechnik GmbH, Germany) with a maximum ozone production capacity of 8 g/h was used for the experiments. A stirred glass reactor (0.5 L) was used to treat sample volumes of 0.4 L. Ozone concentrations in the in-gas and off-gas of the reactor were measured with ozone gas phase analyzers. The in-gas was added at a gas flow rate of 0.4 L/min and an ozone concentration of 10 mg/L (specific ozone dose 1 $gO_3/gDOC$, $k_La = 0.72$ 1/min). Ozone balance profile and information about calculation are presented in Text S1.

All process parameters are collected in Table 1.

2.2. Targeting of ARGs, facultative pathogenic bacteria (FPB) and sampling procedures

The ARGs were chosen as follows: bla_{TEM} (resistance to beta-lactams), *erm*B (resistance to macrolides), *qnr*S (reduced susceptibility to fluoroquinolones), *tet*M (resistance to tetracyclines). ARGs were quantified from metagenomic DNA extracts previously extracted from wastewater samples using quantitative polymerase chain reaction (qPCR) approach [8,14]. While taxonomic gene quantifications of five FPB targeting were chosen and analysed by qPCR as follows: *Escherichia coli (yyc*T*), Pseudomonas aeruginosa (ecf*X*), Klebsiella pneumoniae (glt*A*), Acinetobacter baumannii (sec*E*),* and enterococci (specific 23S rDNA). Moreover, eubacterial 16S rDNA and the integrase gene *intl*1 involved in horizontal gene transfer were investigated. Primer sequences and qPCR parametrs are listed in Table S1. The secondary effluent (CAS) samples were taken from a municipal wastewater treatment plant (WWTP Neureut, Karlsruhe, Germany, 875,000 population equivalents). The physicochemical characteristic parameters of the secondary Neureut effluents are given in Table S2. Samples are taken weekly from April 2021 to April 2022. Water samples were stored at 4 °C and were further processed within 24 h. Effluent filtration and DNA extraction was according to previous procedures [8,14]. Procedure of quantitative analysis of a sample is given in Text S2.

A differentiation of living and dead cells is a significant challenge in efficiency evaluation of treatmet processes including inactivation. After treatments, quantification based on DNA detection by amplification technique can lead to an overestimate the risk of bacterial mtargets or give false-positive results. Thus, propidium monoazide (PMA) is highly recommended to be used in conjunction with a qPCR assay for detection viable cells. This DNA-intercalating PMA agent enabling exclusive detection of viable cells, which is achieved by entering injured or damaged cells characterized by an affected cell membrane potential.

Entered PMA molecules are covalently binding to cellular DNA, which in consequence avert DNA amplification from dead or injured bacteria [36,37]. A PMA concentration of 25 μM was used to suppress qPCR signals from dead or injured cells without impacting viability of intact bacteria.

Moreover, the regrowth potential of the bacteria and its influences on ARGs abundance was investigated. After inactivation, the samples were stored in the absence of light at room temperature for 24 h (photocatalytic inactivation) and 72 h (photocatalytic and catalytic ozonation).

2.3. Photocatalysts

Photodeposition method was used to prepare modified mono and bimetallic (Cu or/and Pd) rutile TiO_2 nanoparticles for enhanced photocatalytic efficiency under visible light. Titanium dioxide P25 Evonik (TiO_2 (P25)) was used as a commercial photocatalyst standard as well.

Urchin-like TiO_2 in form of rutile was prepared according to our previous article [38]. In brief, 68 g of TBOT was introduced to 60 mL of concentrated HCl. After 10 min. of stirring the mixture was transferred into a Teflon-lined stainless-steel autoclave and heated at 170 °C for 24 h. When the reactor cooled to room temperature, the reaction mixture was washed several times with water and ethanol, dried at 70 °C, and calcined at 300 °C for 1 h.

On the material prepared in as described above, mono and bimetallic nanoparticles were deposited using the photodeposition method. An appropriate amount of photocatalysts and metal precursor aqueous solution (potassium tetrachloropalladate (II), copper diacetate monohydrate) was mixed with 60 mL of ethanol. The mixture was transferred to a quartz glass photoreactor with 80 mL of total volume. The final mixture was mixed in the dark for 0.5 h and the headspace of the reactor degasified with nitrogen for 1 h. After that, the reactor was irradiated using Xenon lamp (Oriel, 1000 W) at 10 °C for 1 h. The product was washed several times with water and ethanol and centrifuged at 6000 rpm. Finally, the product was dried at 60 °C for 12 h.

The abbreviations for various photocatalysts used in the present study are listed in Table 2.

2.4. Photocatalysts characterization

Diffuse reflectance spectra were recorded on a UV–vis spectrophotometer (UV 2600, Shimadzu) equipped with an integrating sphere using a $BaSO_4$ reference. Phase composition was analyzed by pXRD using a Bruker D8 Advance Eco diffractometer (Cu Kα) equipped with a LynxEye-XE detector. The collected data were analysed by the Le Bail method using HighScore Plus ver. 3.0e software. Morphology was investigated by field-emission scanning electron microscopy (FE-SEM; JEOL JSM-7610F). Raman spectra were carried out at room temperature using a Thermo Scientific DXR Smart Raman spectrometer with a 532 nm laser. High angle annular dark-field scanning TEM (HAADF-STEM) combined with EDXS was used to investigate the chemical composition of the TiO_2 – 0.5 wt. %Cu – 0.5 wt. %Pd nanoparticles (NPs). The experiments are performed on a FEI Osiris ChemiSTEM microscope at 200 keV electron energy, which is equipped with a Super-X EDXS system comprising four silicon drift detectors. EDXS spectra are quantified with

Table 1

Complete configuration options for the experiments, including parameters of different approaches (matrix: municipal secondary effluent from a conventional activated sludge (CAS) system; specific ozone dose: 1 $gO_3/gDOC$; Xenon lamp as a light source, catalysts concentration: 200 mg/L).

Experiment		Working volume, mL	Time, h	Light
Photocatalytic inactivation	Cat./Vis	200	1 2 3	+
	Bacterial			
Regrowth	200	24	–	
Photocatalytic ozonation (TiO₂-CuPd)	Cat./O₃/Vis	400	2	+
Ozonation	O₃	400	2	–
Photolytic ozonation	O₃/VIS	400	2	+
Photocatalytic ozonation (TiO₂-Cu; TiO₂-CuPd)	Cat./O₃/Vis	400	2	+
	Bacterial regrowth	200	72	–
Catalytic ozonation (TiO₂-Cu; TiO₂-CuPd)	Cat./O₃	400	2	–
	Bacterial regrowth	200	72	–

Cat.– catalyst.

Table 2

Nominal compositions and abbreviation for photocatalysts tested in present study.

Photocatalyst with nominal metal content	Nomenclature
TiO₂ P25 nanoparticles	TiO₂ (P25)
TiO₂ rutile nanostructure	TiO₂ (rutile)
TiO₂ rutile nanostructure modified by 0.5 wt% Cu	TiO₂-Cu
TiO₂ rutile nanostructure modified by 0.5 wt% Pd	TiO₂-Pd
TiO₂ rutile nanostructure modified by 0.5 wt% Cu and 0.5 wt% Pd	TiO₂-CuPd

the FEI software package "TEM imaging and analysis" (TIA) version 4.7 SP3. Using TIA, element concentrations were calculated on the basis of a refined Kramers' law model, which includes corrections for detector absorption and background subtraction. For this purpose, standard-less quantification, i.e. by means of theoretical sensitivity factors, without thickness correction was applied. EDXS spectra obtained during scanning of a rectangular area including inside a single NP are used to determine the average chemical composition of nanoparticles. The quantification of Ti-, Cu-, Pd- and O-content from EDXS area scans was performed by using the Ti-K, Cu-K and Pd-L series, as well as, the O-K_α line. Besides the EDXS lines of the corresponding elements, i.e. lines of the Ti-K, Cu-K and Pd-L series, as well as, the O-K_α line, X-ray lines of: Cu-L and Ti-L series from nanoparticles, which are not used in the EDXS analysis, the Mo-K and Mo-L series from the clamp device, Al-K lines from the anti-twist ring, Au-L and Au-M series from the grid and C-K_α line from the amorphous carbon substrate are also observed in all EDXS spectra. Additionally, EDXS elemental maps of Ti (Ti-K_α line), Cu (Cu-K_α line), Pd (Pd-L_α line) and O (O-K_α line) are recorded and used to investigate their distribution within the sample.

The analysis of the catalysts surface chemical composition and the speciation of the existing elements was performed with X-ray photoelectron spectroscopy (XPS) with the application of Kratos Axis Ultra spectrometer with the Al Kα X-ray source (1486.6 eV). The spectra were registered in regions characteristic for titanium (Ti 2p, 470–450 eV), oxygen (O 1 s, 540–520 eV), palladium (Pd 3d, 350–330 eV), and copper (Cu 2p, 970–910 eV), with a step width of 0.1 eV. The survey spectra were also recorded in the binding energy range between 1200 and −5 eV, with a step width of 1 eV. The chemical composition was calculated as an average value determined from three spots on the surface of the samples. Spectra were subjected to background subtraction with Shirley's function and deconvolution with the Kratos Vision 2 software. All components in the spectra were fitted with the Gauss-Lorentz combined function (30:70). Moreover, spectra were recorded with the application of the surface charge neutralizer.

The reusability of the bimetallic catalysts have been analyzed during photocatalytic oxidation and photocatalytic ozonation of tetracycline (more information can be found in SI). The metal content in the solution (possible leaching) was determined by an inductively coupled plasma-optical emission spectroscopy instrument (ICP-OES, Agilent Technologies, ICP-OES 5110, Waldbronn, Germany).

3. Results and discussion

3.1. Characterisation of photocatalyst

Before evaluation of the photocatalytic inactivation activity of obtained nanocomposites, the characterization of mono- and bimetallic TiO$_2$-metal photocatalysts in comparison to pure TiO$_2$ (P25) and modified pristine rutile TiO$_2$ as a reference were performed.

Morphology of obtained pristine TiO$_2$ (rutile) and modified TiO$_2$ photocatalysts is presented in Fig. 1. SEM images revealed that both pristine and modified TiO$_2$ had the same shape in form of spheres. Each sphere was composed of plenty individual square rods, recalling this way sea urchins. In each obtained sample, an average diameter of the spheres reached 6.1 $\pm$ 0.45 μm. Individual rods showed dimensions from 20 to 90 nm (square side length). Referring to reference TiO$_2$ (P25), from spherical to polygonal shapes with an average particle size of 25 $\pm$ 4 nm were observed. Due to small size and homogeneity of samples, Pd, Cu, and CuPd NPs could not be seen on SEM images.

To better characterize the distribution of Cu and Pd on the synthesized particles HAADF STEM was used. Fig. 2 shows the images of TiO$_2$-CuPd with a formation of elongated TiO$_2$ particles decorated with quasi-spherical CuPd particles. The contrast of HAADF-STEM images, which is mainly related to the atomic number (Z) of chemical elements in the material, besides the local thickness of particles, make them well-suited to distinguish particles containing atoms with different Z. Accordingly, the image shows a clear contrast difference between the quasi-spherical particles consisting of heavier Cu and Pd elements with a bright contrast and the elongated TiO$_2$ particles composed of light Ti and O elements with a dark contrast (Fig. 2).

An elemental analysis also verified the inclusion of Cu and Pd in the composites. As can be observed in Fig. S1, the EDXS spectrum of the bimetallic catalyst had peaks for Cu, Pd, as well as C, Ti, and O. The EDXS map of the Cu and Pd distribution indicates that quasi-spherical particles with diameters D of 5 nm $\leq$ D $\leq$ 50 nm are composed of a Pd-rich Pd-Cu alloy. Almost the entire Pd is contained within such particles. Compared to that, only a small part of Cu can be found in nanoparticles. Most part of Cu are distributed on the surface of the elongated TiO$_2$ particles, as a fine distribution of very small CuPd particles with diameters of D $\leq$ 2–3 nm, which are composed of a CuPd alloy. EDXS area scan analysis of 93 different NPs confirms the formation of nanoparticles composed of homogeneous PdCu alloys. Moreover, it shows that the Cu composition decrease (Pd composition increase) with increasing the particle size for particle diameters D of D $\leq$ 20 nm (Fig. 2, Fig. S1). Larger particles with diameters D greater than 20 nm have about the same composition.
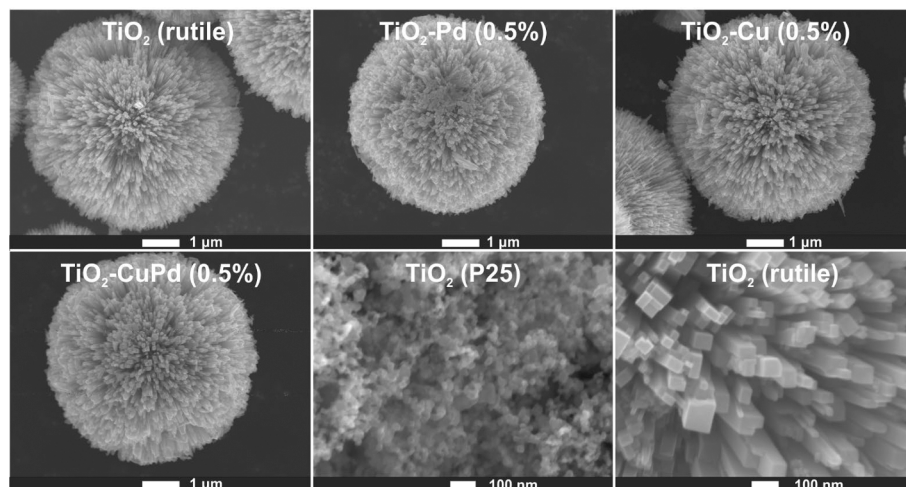

Fig. 1. SEM images of pristine TiO$_2$ (rutile and P25) and modified TiO$_2$ photocatalysts.
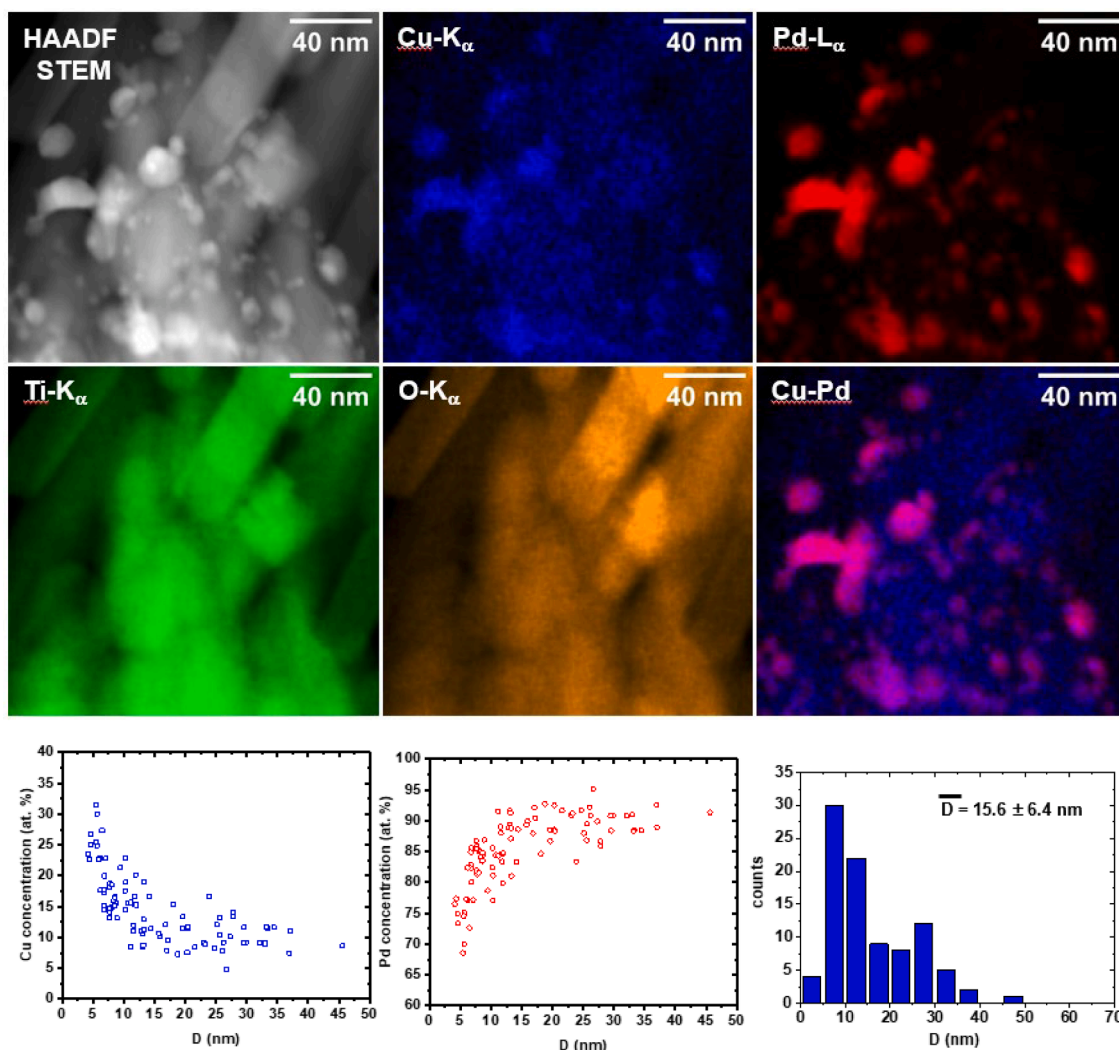
Fig. 2. HAADF-STEM image and EDXS maps of Cu (Cu-Kα line - blue), Pd (Pd-Lα line - red), Ti (Ti-Kα line - green), O (O-Kα line - orange) and CuPd distributions; Chemical composition of CuPd nanoparticles as a function of their diameter and histogram of size distribution. (For interpretation of the references to colour in this figure legend, the reader is referred to the web version of this article.)

As determined by the XPS analysis, the surface of the catalysts consists of Ti, O, Pd, and Cu. All spectra are presented in Fig. S2. The content of titanium and oxygen in the samples is similar: 71.53 – 73.12 at.% of oxygen and 25.65 – 28.11 at.% of titanium, respectively (Table 3). The atomic ratio between O and Ti equals 2.54 – 2.85, which is a higher value than the one for ideal TiO_2, namely 2. The slight excess of oxygen can be attributed to the chemisorbed aerial moisture, which increases the oxygen content. The remaining part of the chemical composition is taken by the copper and/or palladium.

Titanium exists mainly at the + 4 oxidation state, which undoubtedly can be assigned to the presence of TiO_2. For TiO_2-Cu and TiO_2-CuPd

samples titanium exists in this form only. In the case of TiO_2-Pd the titanium is slightly reduced because the following titanium speciation was found: 70.3 at.% of Ti^{4+}, 14.7 at.% of Ti^{3+}, and 16.0 at.% of Ti^{2+}. These forms are represented by the components centered at 459.0 eV, 457.3 eV, and 455.9 eV at the Ti $2p_{3/2}$ XPS spectrum [39,40], respectively. All studied Cu-containing samples comprise metallic copper (Cu^0), confirmed by the presence of peaks centered at 932.2 eV($Cu 2p_{3/2}$) and 951.8–951.9 eV ($Cu 2p_{1/2}$) [41,42]. On the other hand, palladium exists in Pd^{2+} and Pd^{4+} oxidation states, assigned by the peaks in the Pd $3d_{5/2}$ spectra, near 336 eV and 338 eV [43,44], respectively. The forms are most probably connected with the existence of PdO and PdO_2, respectively.

The XPS results suggest that the content of copper is ca. 4 times higher than the content of palladium. EDXS maps showed that the concentration of copper increases with the decrease of the CuPd nanoparticles distributed onto the rutile. Combining the conclusions from the two methods one can conclude that copper is distributed mainly onto the surface of the CuPd nanoparticles, whilst palladium is present mostly in the deeper parts of the NPs. XPS probes the samples at the depth of 10–15 nm and an area of 700 × 300 µm. Therefore, the chemical composition shown in Table 3 should be considered as a description of the surface of both phases: rutile and metallic nanoparticles.

Crystallographic analysis by Raman spectroscopy and X-ray

Table 3
Chemical composition determined with XPS (expressed in atomic %).

Sample	Copper	Palladium	Titanium	Oxygen	O/Ti	Cu/Pd
TiO_2 – Cu (0.5%)	0.36 ± 0.3	*Not found*	28.11 ± 0.46	71.53 ± 0.26	2.54	
TiO_2 – Pd (0.5%)	*Not found*	0.42 ± 0.19	27.39 ± 0.42	72.19 ± 0.28	2.64	
TiO_2 – CuPd (0.5%)	0.98 ± 0.27	0.24 ± 0.01	25.65 ± 1.64	73.12 ± 1.38	2.85	4.08

diffraction confirmed the rutile phase of synthesized TiO₂ nanostructure (Fig. S3). Pristine TiO₂ (rutile) as well as modified TiO₂ samples exhibited identical spectral line shape (Fig. S3 left) with weak and strong bands at 143 (B1g), 238 (two-photon scattering of rutile), 443 (Eg) and 608 (A1g) 1/cm assigned to active modes [45]. Raman spectra of TiO₂ (P25) exhibited all the features typical of this form of TiO₂ [46]. These characteristic vibrational frequencies at 134, 382, 500, and 618 1/cm confirmed the presence of anatase phase in P25. All diffraction peaks observed for the pristine TiO₂ (rutile) as well modified TiO₂ samples are derived from rutile phase of TiO₂ (rutile) (Fig. S3 right). The strongest signal at $2\theta = 27.3°$ is corresponding to reflection from the (1 1 0) plane. The next diffraction peaks at $2\theta = 36.0, 39.1, 41.1, 44.0, 54.2, 56.6, 62.7, 64.0$ and $69.0°$ correspond to (1 0 1), (2 0 0), (1 1 1), (2 1 0), (2 1 1), (2 2 0), (0 0 2), (3 1 0), and (1 1 2), respectively [47]. Lattice parameters of the rutile structure (P42/mnm) were estimated based on the Le Bail method. For pristine TiO₂ (rutile) and modified TiO₂ samples the same values were obtained, namely, $a = 4.5955(1)$ Å and $c = 2.9581(1)$ Å. These values were very close to those reported in the literature ($a = 4.5924$ Å and $c = 2.9575$ Å) [48]. Importantly, deposition of Pd, Cu or CuPd nanoparticles onto TiO₂ did not change the crystal structure of TiO₂. In the sample TiO₂ (P25), in addition to rutile, the anatase phase was found which is in line with the literature [49].

Diffuse reflectance UV–Vis spectroscopy was used to access the optical properties of synthesized catalysts. Fig. 3A shows DRS UV–Vis spectra of pristine TiO₂ (rutile and P25) and modified TiO₂ photocatalysts. The highest absorption of light was observed in the range of 250–420 nm, which agrees with the rutile phase (for pristine and modified urchin-like TiO₂). Decoration of urchin-like TiO₂ by Pd, Cu and CuPd nanoparticles allowed the absorption range to be extended into the visible made it possible to extend the absorption of irradiation more towards the visible range. In the cause of TiO₂-Cu sample, extended absorption in the 420–550 nm is due to direct charge transfer from the valence band of TiO₂ to Cu [50–52]. Loading of Pd nanoparticles on to TiO₂ (rutile) or TiO₂-Cu samples significantly affected the optical properties in the visible range, which is related with the grey colour of these samples [53,54]. Such observation was reported in the literature previously [55,56].

The PL spectra (Fig. 3B) shows peaks in the range 2.71–2.81 eV corelated with the excitonic e − h + recombination via oxygen vacancies; peak around 2.91 eV attributed to the recombination of free excitons in rutile, but also greater than 3 eV that is ascribed the band-to-band e^--h^+ recombination [38,57] When compared to pristine TiO₂ (rutile), the PL intensity of both TiO₂-Cu and TiO₂-Pd is significantly quenched. When bimetallic catalysts are considered the PL intensity is even lower then monometallic catalysts indicating an inhibition in electron-hole recombination rate that may cause higher photocatalytic activity. In all cases, the decrease in PL intensity suggests a diminished radiative recombination also in the range typically attributed to surface state-mediated recombination (2.1–2.7 eV) [16].

One of the most important practical aspect of photocatalytic based processes is the catalysts stability. Thus, experiments of multiplate reuse of TiO₂-CuPd were carried out for photocatalytic oxidation and photocatalytic ozonation of tetracycline (Text S3, Fig. S10). After four cycles of antibiotic degradation no significant changes can be observed, small differences in pseudo-first order rate constant value are probably due to catalyst weight loss during the recycling process. Moreover, the bimetallic catalysts did not exhibit Cu or Pd leaching during reaction, probably due to the formation of stable CuPd alloy nanoparticles.

3.2. Analysis of biological treated wastewater

The microbiological quality of the WWTP secondary effluent is shown in Fig. 4. Based on analysis, it was found that FPB like enterococci, *E. coli, A. baumanni, K. pneumoniae,* and *P. aeruginosa* can be detected in high abundances (5.46×10^3 cell equivalents / 100 mL, 1.75×10^3 cell equivalents / 100 mL, 2.12×10^3 cell equivalents / 100 mL, 6.48×10^3 cell equivalents / 100 mL, and 3.33×10^2 cell equivalents / 100 mL, respectively). Moreover, four frequently detected antibiotic esistance genes associated with WWTP effluents, i.e. *bla*TEM, *tet*M, *erm*B, and *qnr*S were analyzed. Herein the median of the genes *bla*TEM (β-lactam resistance) with 1.95×10^4 cell equivalents / 100 mL, *tet*M (tetracycline resistance) with 1.68×10^4 cell equivalents / 100 mL, *qnr*S (quinolone resistance) with 2.06×10^4 cell equivalents / 100 mL, and *erm*B (erythromycin resistance) with 1.17×10^4 cell equivalents / 100 mL are presented. As can be seen the abundance of ARGs and FPB was not stable during the sampling campaign time. The statistic analysis clearly shows that depending on the target the abundance could differ by even more than 1 log unit. The higher fluctuation in abundance has been observed during spring and summer season leading to increase mean values (outliers data in Fig. 4). While in fall and winter abundance
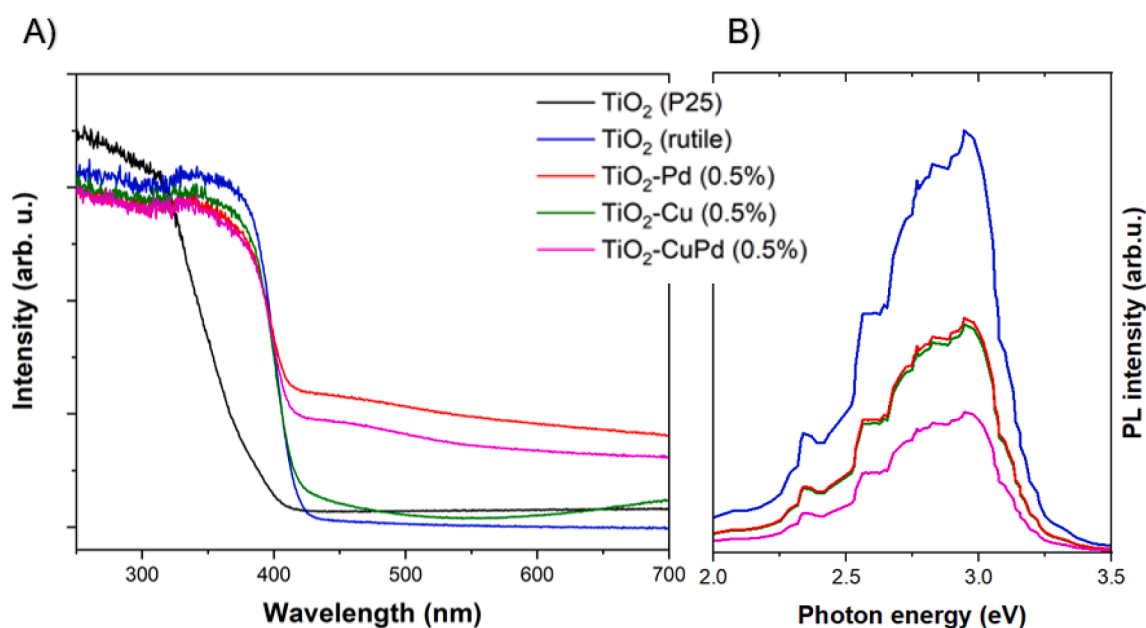

Fig. 3. A) DRS UV–Vis spectra of pristine TiO₂ (rutile and P25) and modified TiO₂ photocatalysts, B) Photoluminescence spectra of synthesized catalysts ($\lambda_{ex} = 315$ nm).
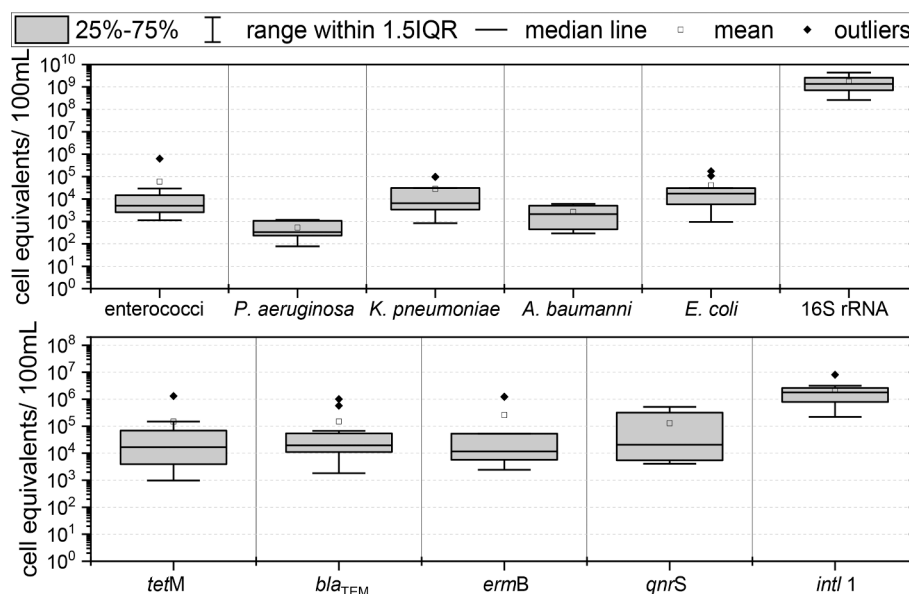
Fig. 4. Cell equivalents of facultative pathogenic bacteria (upper graph) and antibiotic resistance genes (lower graph) analyses in secondary effluents during one year sampling campaignes. Outliers of the spring and summer campaign are indicated by specific signs (◆).

was more stable, which is represented by median values (Fig. 4). The eubacterial 16S rRNA gene marker, as well as *intl*1 profiles indicate stability in abundance during all year. 16S rRNA genes and *intl*1 ́fgenes were present at an abundance of 1.35×10^9 cell equivalents / 100 mL and 1.80×10^6 cell equivalents / 100 mL, respectively.

3.3. Efficiency of photocatalytic treatment

The photocatalytic performance has been evaluated for tetracycline decomposition. The apparent quantum efficiencies are presented in Table S3. It is indicated that the photocatalytic activity of the bimetallic catalyst shows a quantum efficiency up to 11% higher compared with monometallic catalysts (7.5% for TiO_2-Pd and 3.8% for TiO_2-Cu) under visible light. Such photocatalytic behavior makes TiO_2-CuPd a promising visible light photocatalyst. The catalytic activity of all synthesized catalysts is highly improved, which is in agreement with their absorption in the visible range presented by diffuse reflectance spectra (DRS) results compared to TiO_2 (P25) (Fig. 3A) or PL spectra (Fig. 3B).

The photocatalytic inactivation with the application of all photocatalysts and the resulting regrowth are presented as cell equivalents of ARGs per 100 mL of filtrated effluent in Fig. S4 and Fig. S5. The summarized data of ARGs inactivation is given in Table 4.

3.3.1. Efficiency of pristine TiO_2 photocatalytic treatment
The comparison of pristine TiO_2 matrix (P25 and TiO_2 (rutile)) clearly shows that rutile form despite higher ability to absorb visible light does not exhibit better removal properties toward ARGs or FPB (Fig. S4A, B and Fig. S5A, B, respectively). Slightly lower bla_{TEM} and *erm*B gene abundances were detected after treatment with TiO_2 (rutile) (1.23 and 2.78 Log Removal Value (LRV), respectively) compared to TiO_2 (P25) (1.54 and 2.87 LRV, respectively) treatment (Table 4). A stronger reduction difference was observed for *qnr*S between TiO_2 (P25) and TiO_2 (rutile) treatment (2.27 and 1.58 LRV, respectivly). Only in case of *tet*M slightly better inactivation by TiO_2 (rutile) treatment than TiO_2 (P25) was observed (1.78 and 1.30 LRV, respectivly). As previously described the resistance gene bla_{TEM} demonstrated to be a more resistant or robust ARG for photocatalytic inactivation treatment, which might depend on the carrier organism [24]. In addition, beside the bla_{TEM} the inactivation of *tet*M gene was also much lower compared to *qnr*S and *erm*B genes. Significant difference (1 log unit) was observed for *intl*1 between TiO_2 (P25) (1.71 log removal) and TiO_2 (rutile) (0.70 log

removal) tratment. However, it should be noted that *intl*1 genes can even increase after the treatment because *intl*1 can be easily acquired by HGT [58]. The lowest inactivation was observed for 16S rRNA gene, however slightly higher efficiency is obtained by TiO_2 (P25) than TiO_2 (rutile) (Table 4). In photocatalytic TiO_2 (P25) treatment ˙OH is the main oxidant, while the rest ROS play a minor role (Text S4). When rutile-based catalyst is considered, a different mechanism of action occurs. The ˙OH radicals are predominantly reactive on the surface of the rutile catalyst and their reactivity in the solution is rather low. Additionally, other ROS are becoming more relevant since rutile has a lower capacity than anatase to create ˙OH radicals through holes (Text S4). As a result, rutile also favours the formation of $^1O_2$ and promotes the production of H_2O_2 (which involves O_2 reduction and the subsequent oxidation of superoxide) [59]. Despite much lower oxidation potential of $O_2^{·-}$, $^1O_2$, H_2O_2 than ˙OH, TiO_2 (rutile) was rather successful in ARGs and FPB removal leading that those ROS may cause significant DNA damage.

3.3.2. Efficiency of mono and bimetallic TiO_2 photocatalytic treatment
After metal modification by copper or/and palladium of rutile carrier, the catalysts give much higher ARGs inactivation efficiencies (Fig. S4C–E; Table 4). Considering mono-metallic catalyst, TiO_2-Cu gives slightly higher *erm*B removal efficiency than TiO_2-Pd (3.19 and 2.70 LRV, respectively). When *tet*M and *qnr*S were considered, TiO_2-Pd led to more than 1 log lower removal capacities compared to TiO_2-Cu (Table 4). The opposite trend was observed for bla_{TEM}, where slightly higher inactivation was detected after TiO_2-Pd rather than for TiO_2-Cu (2.08 and 1.89 LRV, respectively).

When monometallic catalysts were compared (Fig. S4C, D, Fig. S5C, D, Table 4), TiO_2-Cu resulted in higher removal than TiO_2-Pd. The higher efficiency of TiO_2-Cu can be related to the higher antimicrobial ability of copper rather than palladium [60]. However, the differences in absorption ability (Fig. 3) and catalysts action are also relevant. As it was shown, the TiO_2-Pd catalysts are strongly activated in the visible region and their action is mostly related to ˙OH formation. While TiO_2-Cu absorbance spectrum overlapped with TiO_2 (rutile) in the range below 400 nm, and its ability to absorb visible light is much lower (Fig. 3). However, the photocatalytic activity at a wavelength higher than 500 nm can be attributed to the plasmonic effect of Cu nanoparticles, where only the excitation through the Cu plasmonic band occurs [53]. Furthermore, acceleration in performance can be explained by copper enhancement of migration of electrons from the conduction

Table 4

Relative abundance and log removal values of ARGs, *intl* 1 and 16S rRNA after different treatment strategies. Reduction higher than 2 log units are bolded.

Target	treatment	Abundance after treatment cell equivalents / 100 mL	Log removal values (LRV)
bla_{TEM}	TiO$_2$ (P25)	$(1.21 \pm 0.21) \times 10^4$	1.54
	TiO$_2$ (rutile)	$(2.47 \pm 0.07) \times 10^4$	1.23
	TiO$_2$-Cu	$(5.41 \pm 1.78) \times 10^3$	1.89
	TiO$_2$-Pd	$(3.41 \pm 2.35) \times 10^3$	2.08
	TiO$_2$-CuPd	$(2.63 \pm 0.26) \times 10^3$	2.20
*erm*B	TiO$_2$ (P25)	$(8.55 \pm 1.17) \times 10^2$	2.87
	TiO$_2$ (rutile)	$(1.04 \pm 0.57) \times 10^3$	2.78
	TiO$_2$-Cu	$(4.08 \pm 1.17) \times 10^2$	3.19
	TiO$_2$-Pd	$(1.26 \pm 0.36) \times 10^3$	2.70
	TiO$_2$-CuPd	$(2.47 \pm 1.77) \times 10^1$	3.58
*tet*M	TiO$_2$ (P25)	$(3.91 \pm 0.99) \times 10^3$	1.30
	TiO$_2$ (rutile)	$(1.29 \pm 0.59) \times 10^3$	1.78
	TiO$_2$-Cu	$(3.87 \pm 0.77) \times 10^1$	3.30
	TiO$_2$-Pd	$(1.84 \pm 0.14) \times 10^3$	1.63
	TiO$_2$-CuPd	$(2.31 \pm 0.14) \times 10^1$	3.53
*qnr*S	TiO$_2$ (P25)	$(1.15 \pm 0.34) \times 10^3$	2.27
	TiO$_2$ (rutile)	$(5.72 \pm 1.55) \times 10^3$	1.58
	TiO$_2$-Cu	$(2.08 \pm 0.66) \times 10^1$	4.01
	TiO$_2$-Pd	$(2.18 \pm 0.34) \times 10^2$	3.00
	TiO$_2$-CuPd	$(1.64 \pm 0.36) \times 10^2$	3.94
intl 1	TiO$_2$ (P25)	$(8.01 \pm 0.82) \times 10^4$	1.71
	TiO$_2$ (rutile)	$(8.15 \pm 0.95) \times 10^5$	0.70
	TiO$_2$-Cu	$(7.17 \pm 1.76) \times 10^3$	2.76
	TiO$_2$-Pd	$(2.37 \pm 0.18) \times 10^4$	2.24
	TiO$_2$-CuPd	$(9.77 \pm 0.46) \times 10^3$	2.63
16S rRNA	TiO$_2$ (P25)	$(2.75 \pm 0.03) \times 10^8$	0.49
	TiO$_2$ (rutile)	$(1.41 \pm 0.05) \times 10^9$	0.37
	TiO$_2$-Cu	$(1.16 \pm 0.01) \times 10^8$	0.87
	TiO$_2$-Pd	$(2.11 \pm 0.01) \times 10^8$	0.61
	TiO$_2$-CuPd	$(1.03 \pm 0.04) \times 10^7$	2.32

band (CB) of TiO$_2$ to Cu by promoting separation of the e/h$^+$ couples and creating a potent electron-sink effect [61–63]. In the presence of copper nanoparticles, O$_2^{\cdot-}$ generated from reduction sites on can be also effectively converted into H$_2$O$_2$ [61]. Simultaneous generation of O$_2^{\cdot-}$, ^{1}O$_2$, H$_2$O$_2$ and $^\cdot$OH in TiO$_2$-Cu photocatalytic treatment, enhanced ARGs and FPB removal compared to TiO$_2$-Pd where its production is limited and $^\cdot$OH is the main pathway.

The photocatalytic inactivation with bimetallic catalysts TiO$_2$-CuPd gives the highest (more than 2 log units removal) efficiency for almost all targets (bla_{TEM}, *erm*B, *tet*M, *intl* 1, and 16S rRNA). However, the efficiency for *qnr*S was similar to that obtained after TiO$_2$-Cu (Table 4).

The synergistic impact of Pd and Cu is probably responsible for the acceleration in ROS generation during TiO$_2$-CuPd/VIS photocatalytic treatment (Fig. S6A). When transition metal Cu serves as an electron sink, encourages charge separation, and increases the amounts of accessible electrons for reduction reactions [31,32,64], which leads to O$_2^{\cdot-}$, ^{1}O$_2$, H$_2$O$_2$ generation. While plasmonic Pd broadens the range of light absorption from the UV to visible region, which is advantageous to charge creation that increases the $^\cdot$OH production. The enhanced $^\cdot$OH generation and presence of another ROS result in higher inactivation efficiency. The improvement of the treatment is observed especially for *tet*M and *erm*B (5.53 and 3.58 LRV, respectively) in comparison to palladium catalyst (1.63 and 2.70 LRV, respectively) and cooper catalyst

(3.30 and 3.19 LRV, respectively). There is no significant difference for *qnr*S between TiO$_2$-Cu and TiO$_2$-CuPd (4.01 and 3.94 LRV, respectively). However, improvement is noticeable for TiO$_2$-Pd (3.0 LRV). We can suspect that *qnr*S favours the TiO$_2$-Cu mechanism rather than a synergistic mechanism of CuPd. As it was discussed above, bla_{TEM} was the most resistant to photocatalytic inactivation. An improvement has been observed for TiO$_2$-Cu (1.89 LRV) and TiO$_2$-Pd (2.08 LRV) and bimetallic TiO$_2$-CuPd (2.20 LRV) photocatalytic treatment compared to pristine TiO$_2$ (P25) (1.54 LRV) and TiO$_2$ (rutile) (1.23 LRV). Based on obtained results it can be assumed that bla_{TEM} is more susceptible to $^\cdot$OH action than O$_2^{\cdot-}$, ^{1}O$_2$, H$_2$O$_2$, therefore remarkable improvement is not observed when for TiO$_2$-Cu and TiO$_2$-CuPd are applied.

The photocatalytic inactivation (with application of modified catalysts) was able to successfully reduce *A. baumannii* and *P. aeruginosa* below the limit of detection (LOD) (Fig. S5). It can be suspected that inactivation of *A. baumannii* and *P. aeruginosa* is strongly related with high sensitivity toward visible light inactivation, that has also been indicated by Hoenes [65]. Lower susceptibility of *E. coli,* enterococci, and *K. pneumoniae* to visible light as well as photocatalytic inactivation resulted in incomplete inactivation. [65] shows inactivation efficiency strongly depend on light wavelength [65]. Under 405 nm irradiation the highest inactivation was found for *A. baumannii, P. aeruginosa, E. coli, K. pneumoniae,* and the lowest for enterococci. While under 450 nm the inactivation efficiency has changed as follows *A. baumannii, P. aeruginosa,* enterococci*, K. pneumoniae,* and *E. coli*. It is known, that during photocatalytic inactivation the light impact plays an indirect role, but predominant inactivation undergoes via photocatalytic action. [66 66] demonstrated that *E. coli* is inactivated particular faster than *K. pneumoniae* under photocatalytic inactivation. While, [7 7] showed that enterococci are much more resistant toward photocatalytic inactivation compared to *P. aeruginosa,* which agrees with our finding.

Despite quite good reduction efficiency for TiO$_2$-CuPd and TiO$_2$-Cu, the abundances of each target increased after dark treatment due to considerable regrowth of bacteria. Nevertheless, for ARGs the initial abundance of the secondary effluent was never reached. The remarkable antimicrobial effect of bimetallic catalysts can be also noticed in case of regrowth experiment when 16S rRNA gene is considered (Fig. S4E). It can be suspected that due to physical cell damage as well as light and ROS action the proliferation does not occurred.

When the kinetics of inactivation is considered (Fig. 5A), it can be seen that 1 h of treatment did not change the abundance of bla_{TEM} and enterococci at all. While, 16S rRNA gene abundance decreased by 2.86 log units. The high 16S rRNA gene removal confirmed that bacteria are more susceptible to inactivation than ARGs. After 2 h of photocatalytic inactivation the inhibition in 16S rRNA gene decay is noticed, while an increased inactivation of bla_{TEM} and enterococci can be seen. Along treatment times a decreasing trend is observed for bla_{TEM}, 16S rRNA gene, and enterococci while in case of *intl*1 gene the abundance decreased during first two hour and increased after 3rd hour after treatment. It became obvious that the community marker genes like the eubacterial 16S rRNA gene present in all bacteria as well as the general *intl*1 gene involved in horizontal gene transfer are not qualified as an indicator for any kind of treatment process including inactivation processes of ARGs. A correlation among the specific kinetics of the selected ARGs and FPB with these bacterial ribosomal or mobile gene markers was not visible. The similar observation was made by Yang et al. [67] after UV inactivation. The increase in *intl*1 abundance may suggests the significantly higher accumulation of MGEs carrying ARGs [68], while inactivation of ARGs were caused by a proper inactivation of hosts [67].

Fig. 5B and Fig. S7 present the relevance of PMA application for evaluation of photocatalytic inactivation. The two different approaches (with and without PMA) were investigated after 2 h of photocatalytic inactivation with TiO$_2$-CuPd indicated visible light irradiation: 1) variable cell identification based on a viability-based qPCR technique (vPCR) - DNA with PMA treatment and 2) and total gene copies detected by qPCR - DNA without adding PMA. Comparing the total (without

PMA) and living (with PMA) samples of the untreated effluent no significant differences are observed for all targets (Fig. 5B and Fig. 7A, B). However, the ratio between viable and non-viable cells caring ARGs is critical for understanding the inactivation mechanisms and enables to predict the risk of bacterial regrowth. The PMA treatment indicated significant differences after photocatalytic inactivation for 16S rRNA gene, enterococci, and *intl*1 gene. There were no relevant differences between the total and viable cell targeting *bla*TEM, indicating a more challenging gene target compared to the removal of the other ARGs. Noteworthy difference in abundances were observed for *tet*M, *erm*B resistance genes as well as *K. pneumoniae*, *E. coli* taxonomic gene markers, (Fig. S7A, B). Significant losses of viable cells were found for all genetic targets under investigation.

3.4. Enhancement of catalytic inactivation combined with ozonation

Based on literature, ozonation is capable to remove FPB, but ozone efficiency toward ARGs is less understood [5,8,10,69,70]. As it was mentioned, the study performed by Alexander et al.; Hembach et al.; and Savin et al. showed, that ozonation has a significant reduction efficiency of 98.4 % against FPB [8–10]. Interestingly when 1 g O_3/gDOC was applied a lower susceptibility toward ozone treatments was found for *P. aeruginosa* [10]. After application of an ozone system (75 g O_3 /Nm^3, contact time 15–30 min.) for FPB inactivation, nonsignificant reduction in *E. coli* and enterococci was observed, whereas *P. aeruginosa* was significantly reduced [9]. Iakovides et al., confirmed that *E. coli* is the most resistant one for ozone treatment [5]. However, the ARB inactivation increased with increasing ozone doses [5,69]. A very high efficiency of FPB and ARG removal were achieved when 50 gO_3 /Nm^3 was applied [70]. The differences in efficiency clearly show that the wastewater matrix has a strong impact on removal capacities. The attempt to apply photocatalytic ozonation (50 gO_3 /Nm$^{3)}$ for ARG inactivation, indicated that TiO$_2$-coated glass Raschig rings and light emitting diodes (LEDs, with dominant λ = 382 nm) was not capable to remove successfully them as well [23]. However, to the best of our knowledge the wider visible light were never investigated for photocatalytic ozonation inactivation regarding ARG inactivation. Considering that TiO$_2$-Cu and TiO$_2$-CuPd catalysts gave the highest ARG inactivation efficiency, it is expected to be the most promising option for photocatalytic ozonation.

As a first step of the investigation, several ozone-based treatments were applied for FPB, ARGs, 16S rRNA and *intl*1 gene removal compared to TiO$_2$-CuPd photocatalytic inactivation (Fig. 6). The ozonation, photolytic ozonation as well as photocatalytic ozonation were capable to remove all FPB below LOD (Fig. 6A).

Considering ARGs inactivation, it was shown that ozonation (O$_3$) led to removal of *tet*M, *qnr*S and *erm*B below LOD. While, *bla*TEM was reduced by 3.22 log. The photolytic ozonation (O$_3$/VIS) was also successful in *qnr*S removal to the LOD. However, *tet*M, *bla*TEM and *erm*B genes were still detected (removal by 3.26, 1.98, 3.62 log unit, respectively (Fig. 6B)). The photocatalytic ozonation (TiO$_2$-CuPd/O$_3$) resulted in highest inactivation efficiency. The *tet*M, *qnr*S and *erm*B were removed under the LOD after photocatalytic ozonation. While, *bla*TEM was removed by 3.23 log unit. For all investigated treatments *bla*TEM was the most resistant ARG. The highest efficiency toward *bla*TEM was achieved after ozonation and photocatalytic ozonation (3.22 and 3.23 LRV, respectively). While similar efficiency was observed for O$_3$/VIS and TiO$_2$-CuPd/VIS (removal by 1.98 and 2.20 LRV, respectively). This can be concluded that the *bla*TEM gene is stronger inactivated by the direct action of ozone than ROS.

When 16S rRNA gene is considered, the best performance was observed for photocatalytic ozonation. The *intl*1 gene were removed by 3.55 log unit after TiO$_2$-CuPd/O$_3$/VIS. Interestingly, the removal of *intl*1 was higher (3.86 log unit) after O$_3$/VIS than that obtained via ozonation (1.07 log units).

The abundance of DNA measurements after treatments clearly shows that TiO$_2$-CuPd/O$_3$/VIS and O$_3$/VIS reduce DNA content to the LOD. Photocatalytic inactivation (no matter 2 or 3 h of treatment) only decreased DNA quantity (Fig. 6A insert). Despite, high ozonation efficiency toward ARGs and FPB, the detection of DNA after ozonation may suggest that some ARGs and ARG carrying bacteria are less susceptible to ozone treatment. It was already found that hosts of the resistance genes *van*A, *bla*VIM, *sul*1, and *tet*G are also resistant or robust to ozone [3].
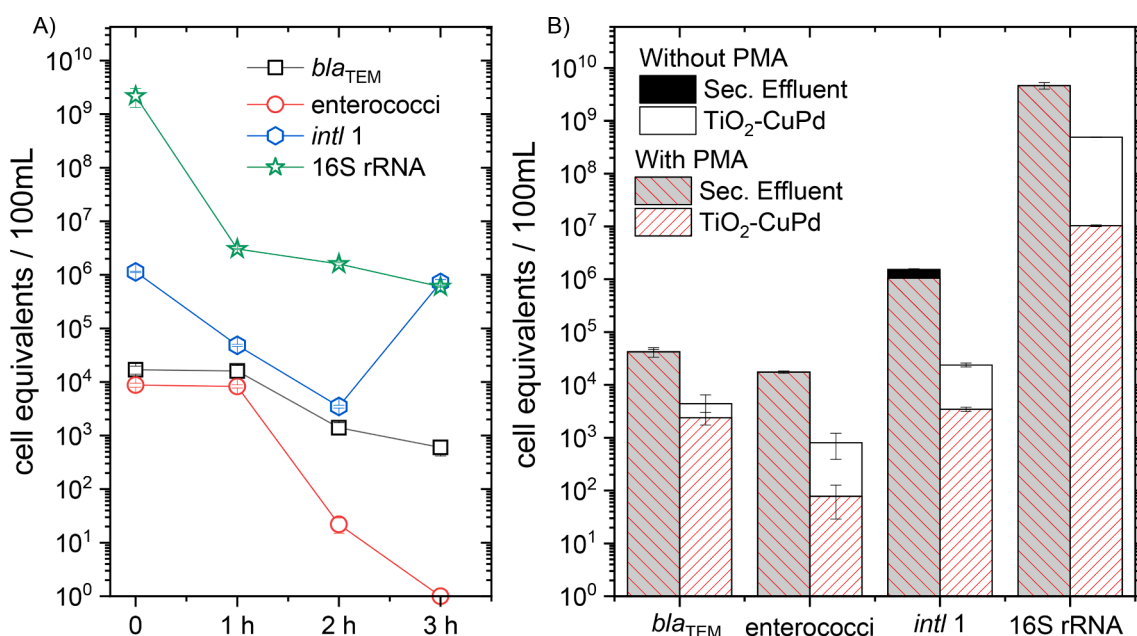

Fig. 5. A) Kinetics of photocatalytic treatment (TiO$_2$-CuPd); B) Abundance of gene targets specific for enterococci, *bla*TEM, 16S rDNA, and intl1 in overall (total) and in viable cells only (viable) in untreated effluent (secondary effluent) and after the TiO$_2$-CuPd photocatalytic inactivation under visible light. The data for PMA treated and untreated secondary effluent sample overlaps in abundance for *bla*TEM, 16S rDNA, and enterococci genes.
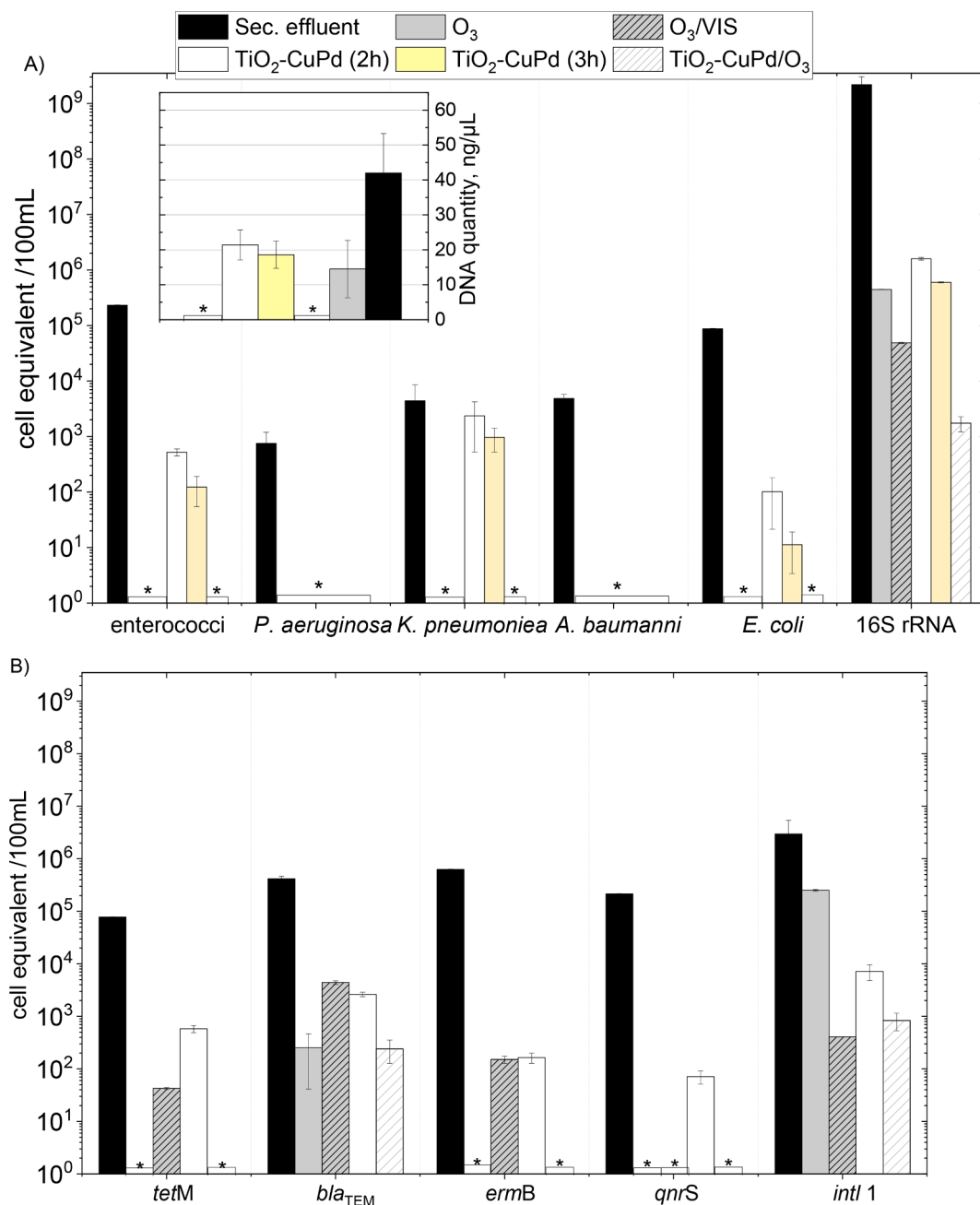
Fig. 6. A) Abundance of gene targets specific for FPB and 16S rDNA, insert: DNA quantity analysis after treatment B) Abundance of ARGs and *intl*1 after advanced treatment inactivation: ozonation (O$_3$), photolytic ozonation (O$_3$/VIS), photocatalytic inactivation (TiO$_2$-CuPd), and photocatalytic ozonation (TiO$_2$-CuPd/O$_3$), * below detection limits (LOD).

3.4.1. Comparison of mono and bimetallic photocatalytic ozonation treatment

In the next step of investigation mono- and bimetallic catalysts were compared during catalytic based processes. The photocatalytic inactivation was confronted with catalytic ozonation and photocatalytic ozonation for copper and copper-palladium TiO$_2$ catalysts. For both tested catalysts the photocatalytic ozonation gives the highest efficiency. The *bla*$_{TEM}$ and enterococci were completely removed with this process (for TiO$_2$-CuPd/O$_3$/Vis and TiO$_2$-Cu/O$_3$/Vis). At the same time, catalytic ozonation leads to only slightly *bla*$_{TEM}$ removal (0.64 and 0.44 log unit removal for TiO$_2$-CuPd/O$_3$ and TiO$_2$-Cu/O$_3$, respectively). However, it should be noted that in this case the treated secondary effluent did have the lowest abundance of FPB and ARGs. Interestingly, catalytic ozonation (without light) was able to reduce 16S rDNA (3.88

and 4.01 log unit removal for TiO$_2$-Cu and TiO$_2$-CuPd, respectively) to a similar level compared to photocatalytic ozonation (4.11 and 4.29 log unit removal for TiO$_2$-Cu and TiO$_2$-CuPd, respectively). Moreover, TiO$_2$-Cu/O$_3$ gives slightly higher *intl*1 gene removal than bimetallic catalysts (2.51 compared to 1.91 log units). Surprisingly the light addition does not accelerate *intl*1 gene removal when TiO$_2$-Cu catalyst was used (2.50 log unit removal). While, photocatalytic ozonation in the presence of TiO$_2$-CuPd resulted in higher *intl*1 gene removal (3.94 log unit removal). Performed studies confirmed that light plays an important role in ARGs inactivation. Furthermore, despite quite well TiO$_2$-Cu performance, the regrowth experiments confirmed that joint action of Pd and Cu nanoparticles due to the different rote of action in the photocatalytic process leads to synergy effects. These synergistic effects can be observed in case of regrowth after photocatalytic inactivation and catalytic ozonation. As

can be seen in Fig. 7 monometallic catalyst (TiO$_2$-Cu) was not able to inhibit the bacterial regrowth compared to bimetallic catalysts (TiO$_2$-CuPd). While, after photocatalytic inactivation as well as catalytic ozonation with application of TiO$_2$-CuPd and 72 h of dark storage, the abundance of all targets were below the initial values. Again, the photocatalytic ozonation leads to the best performant and for both catalysts, the regrowth was inhibited and achieved abundance much below initial levels. The high efficiency of photocatalytic ozonation treatment with bimetallic catalysts was proved for longer time treatment. When the kinetics of inactivation is considered (Fig. S8), it can be seen that 3 h of treatment caused completely removal of *bla*$_{TEM}$, enterococci and *intl*1. While significant improvement was observed for 16S rRNA. Moreover, even 1 h of photocatalytic ozonation treatment led to higher ARGs removal compared to 3 h of photocatalytic treatment (Fig. 5A).

When photocatalytic ozonation mechanism is considered (Fig. S6B, C), the stronger oxidation potential of O$_3$ enables to get electrons from Cu and Pd easier than molecular O$_2$. Through this process, photoexcited electron mobility is increased, and photoexcited electron and hole recombination is decreased. Additionally, O$_3$ would be converted to O$_3^{\cdot-}$ after receiving electrons from Cu which may result in $\cdot$OH generation [30]. At the same time, ozone may react directly or indirectly via the production of $\cdot$OH and H$_2$O$_2$. As it is shown in Fig. S6C, O$_2^{\cdot-}$, ^{1}O$_2$, H$_2$O$_2$ and $\cdot$OH are generated during photocatalytic ozonation. It is known that ROS can assault the cell membrane, damaging coenzyme A and impairing or stopping cellular respiration activity, which can result in cell death [71,72]. The holes can act not only indirectly leading to $\cdot$OH

Fig. 7. Comparison between A) bimetallic TiO$_2$-CuPd and B) monometallic TiO$_2$-Cu action during photocatalytic inactivation (Cat./VIS), catalytic ozonation (Cat./O$_3$), and photocatalytic ozonation (Cat./O$_3$/VIS) and its impact on bacterial regrowth.

generation, but also directly as well as e$^-$ can also play important roles in the photocatalytic bacterial inactivation [63,73]. It was proved that during photocatalytic ozonation inactivation is caused by direct UVA action and chain reactions involved in the process. The photocatalytic ozonation involves O$_3$ which induces DNA breaks and oxidative DNA damage. Unlikely, O$_2^{\cdot-}$ cannot be considered as a ROS responsible for DNA damage due to limitations in crossing biological membranes [74]. Bearing in mind that O$_2^{\cdot-}$ is generated in a very high amount in the presence of Cu nanoparticles and can rapidly react with $\cdot$OH on the conduction band to generate ^{1}O$_2$ or can also react with H$^+$ or h$^+$ on VB to form ^{1}O$_2$. Moreover, O$_2^{\cdot-}$ takes a part in H$_2$O$_2$ generation as well. It is well-known that ^{1}O$_2$ and H$_2$O$_2$ are responsible for DNA damage [74]. Therefore, we assume that not only $\cdot$OH, but also singlet oxygen can be the key ROS responsible for ARGs and FPB inactivation when bimetallic catalyst is considered. However, the superior role of H$_2$O$_2$ can not be neglected.

3.5. Comparition of different catalytic treatment – Regrowth approach

Under visible light, unmodified catalysts (TiO$_2$ (P25) and pristine TiO$_2$ (rutile)) were able to reduce ARGs and FPB despite different mechanism of action. It was found that insufficient removal of ARGs, TiO$_2$-CuPd photocatalysts can significantly remove FPB under visible light conditions (Fig. 8A). After 24 h dark storage bacterial regrowth was observed in case of all investigated catalysts (Fig. 8B). It was conclude that, the presence of VBNC state may be responsible for regrowth after photocatalytic treatment. It can be observed that after TiO$_2$ (rutile) photocatalytic inactivation enterococci reach abundance higher than for untreated effluents. Also *E. coli* abundance was close to initial value.

Application of photocatalytic ozonation resulted in complete FPB and ARGs removal from wastewater effluents when bimetallic and Cu-metallic catalyst was applied (Fig. 8A). Significant differences were observed in bacterial regrowth between with TiO$_2$-Cu and TiO$_2$-CuPd. Catalytic ozonation was not able to prevent the bacterial regrowth of *bla*$_{TEM}$ and *erm*B genes. The *bla*$_{TEM}$ abundance after 72 h dark storage of TiO$_2$-Cu/O$_3$ treated sampels was higher than initial values from untreated effluents (Fig. 8B). At the same time *A. baumannii*, *K. pneumoniae*, and *E. coli* were found to regrowth as well. While, after catalytic ozonation with application of TiO$_2$-CuPd and 72 h of dark storage, the abundance of all targets were below the initial untreated values. The bacterial regrowth of *K. pneumoniae, E. coli*, and enterococci was observed. Slightly higher abundance was also found for *bla*$_{TEM}$ and *erm*B genes.

For both catalysts the regrowth after photocatalytic ozonation was inhibited and achieved abundance much below initial levels. From all ARGs, only *bla*$_{TEM}$ was detected after photocatalytic ozonation. The *bla*$_{TEM}$ abundance was slightly higher after TiO$_2$-CuPd/O$_3$/VIS compared to TiO$_2$-Cu/O$_3$/VIS. It should be noted that after bimetallic photocatalytic ozonation only *K. pneumoniae* regrowth. While during TiO$_2$-Cu/O$_3$/VIS *K. pneumoniae* and *E. coli* were detected.

4. Conclusion

Our study strongly indicated that photocatalytic ozonation has the greatest potential for the removal of facultative pathogenic bacteria and antibiotic resistance genes. Especially, photocatalytic ozonation with the application of TiO$_2$-CuPd resulted in most significant removal of FPB and ARGs. It is suspected that Pd nanoparticles increase the generated charge carriers, while Cu nanoparticles prolonged their lifetime, which leads to acceleration of ozone – catalysts reaction. Despite similar FPB inactivation after ozonation and photocatalytic ozonation, ozone leads to lower DNA destruction, leading possibility of transferring intact and liberated DNA containing ARGs.

From all investigated targets *qnr*S and *tet*M genes seems to be the most sensitive against photocatalytic and catalytic ozonation with TiO$_2$-CuPd and TiO$_2$-Cu catalysts. Despite catalytic ozonation resulted in
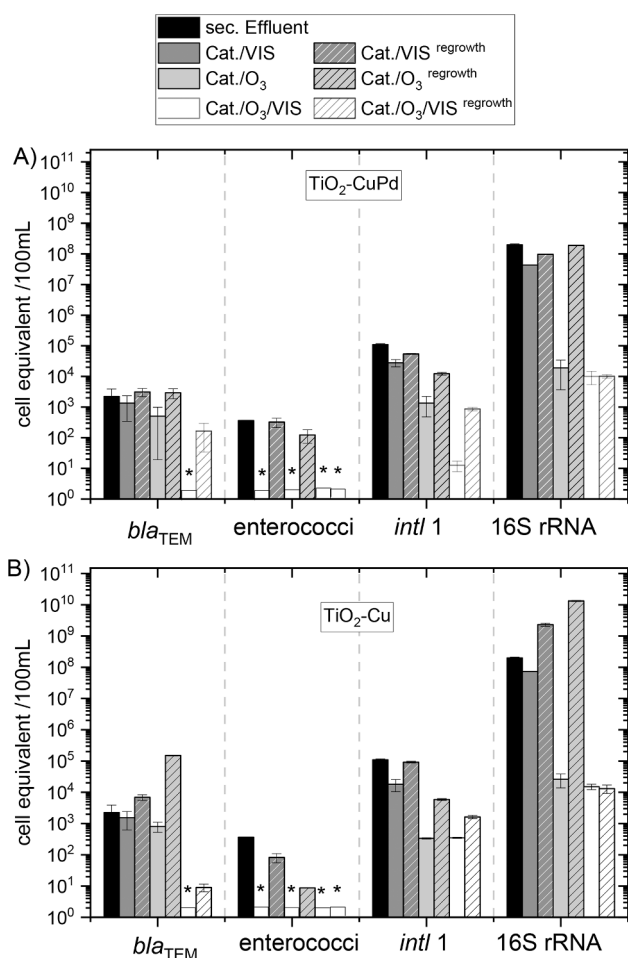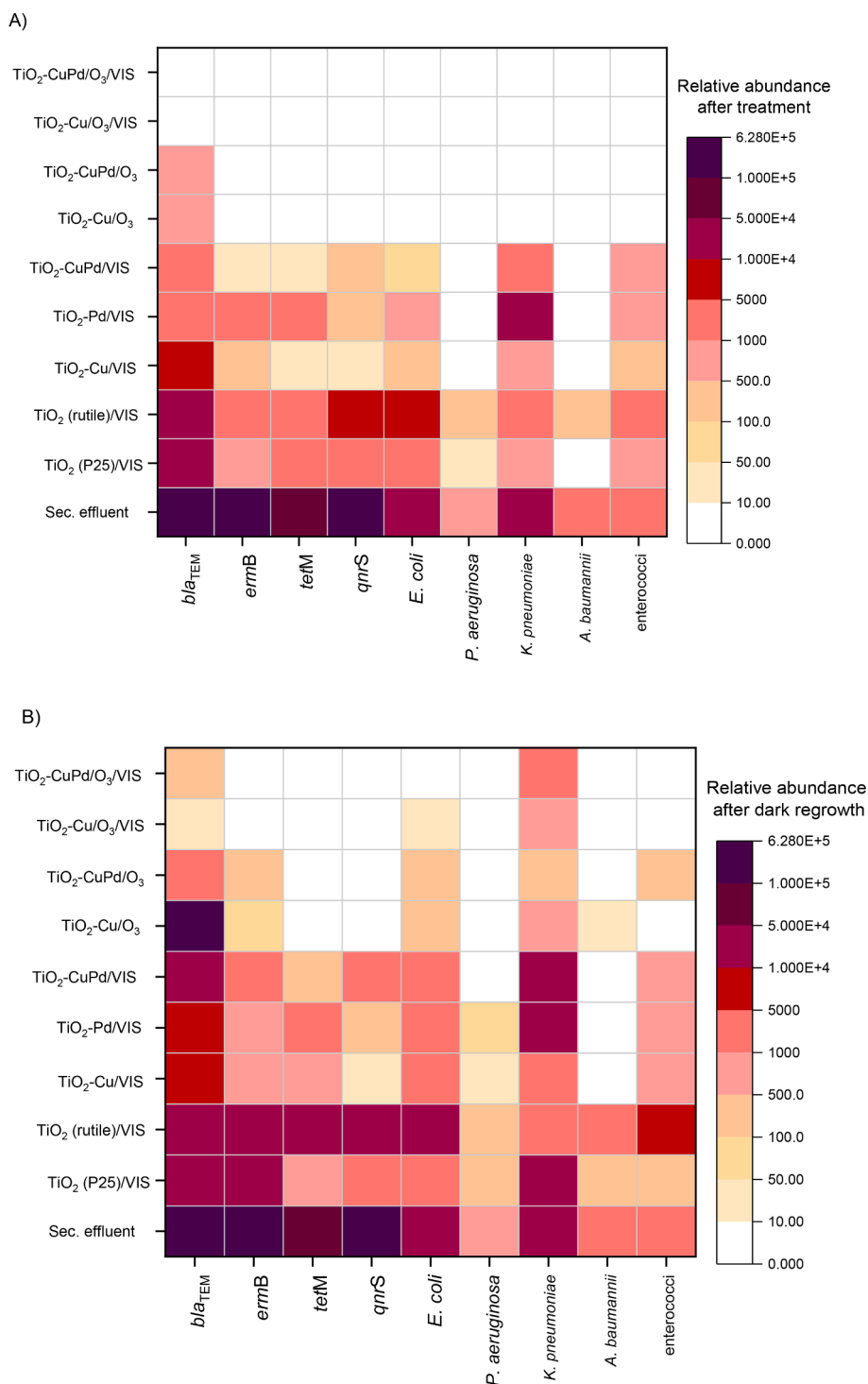
Fig. 8. Heat map of relative abundance of ARGs and FPB:A) after different treatment strategy, B) their bacterial regrowth after 24 h (photocatalytic inactivation) and 72 h (catalytic and photocatalytic ozonation) dark storage.

complete FPB and ARGs removal from wastewater effluents. When bimetallic and Cu-metallic catalyst were used the regrowth for bla_{TEM} and ermB genes were detected. Bacterial regrowth after photocatalytic ozonation allowed to correlate bla_{TEM} and *K. pneumoniae*. The comparison between catalytic ozonation and photocatalytic ozonation, clearly showed that light plays important role in the inactivation of ARGs and bacterial regrowth. It can be assumed that enhancement by light is caused by direct UVA action and chain reactions involved in photocatalytic ozonation process.

The bla_{TEM} and *K. pneumoniae* showed the highest resistance toward photocatalytic inactivation, therefore the efficiency of the photocatalytic based technology may rely on their inactivation.

The study demonstrated that superior photocatalytic ozonation efficiency may be attained under visible light, paving the way to the use of sunlight rather than artificial UV lamps, which would significantly lower the costs and expedite the implementation of the process. It is possible to provide the most effective and economical tertiary treatment for the secondary effluents after applying visible light-induced recyclable heterogeneous photocatalysis (reusable catalyst - elimination of catalyst separation problem) combined with O_3.

Declaration of Competing Interest

The authors declare that they have no known competing financial interests or personal relationships that could have appeared to influence the work reported in this paper.

Data availability

No data was used for the research described in the article.

Acknowledgements

Appendix A. Supplementary data

Supplementary data to this article can be found online at https://doi.org/10.1016/j.cej.2023.142243.

References

[1] D. Calderón-Franco, M.C.M. van Loosdrecht, T. Abeel, D.G. Weissbrodt, Free-floating extracellular DNA: systematic profiling of mobile genetic elements and antibiotic resistance from wastewater, Water Res. 189 (2021) 116592.

[2] S. Rodriguez-Mozaz, I. Vaz-Moreira, S. Varela Della Giustina, M. Llorca, D. Barceló, S. Schubert, T.U. Berendonk, I. Michael-Kordatou, D. Fatta-Kassinos, J.L. Martinez, C. Elpers, I. Henriques, T. Jaeger, T. Schwartz, E. Paulshus, K. O`Sullivan, K.M. M. Pärnänen, M. Virta, T.T. Do, F. Walsh, C.M. Manaia, Antibiotic residues in final effluents of European wastewater treatment plants and their impact on the aquatic environment, Environ. Int. 140 (2020) 105733.

[3] K. Slipko, D. Reif, H. Schaar, E. Saracevic, A. Klinger, L. Wallmann, J. Krampe, M. Woegerbauer, P. Hufnagl, N. Kreuzinger, Advanced wastewater treatment with ozonation and granular activated carbon filtration: inactivation of antibiotic resistance targets in a long-term pilot study, J. Hazard. Mater. 438 (2022), 129396, https://doi.org/10.1016/j.jhazmat.2022.129396.

[4] M. Gmurek, E. Borowska, T. Schwartz, H. Horn, Does light-based tertiary treatment prevent the spread of antibiotic resistance genes? Performance, regrowth and future direction, Sci. Total Environ. 817 (2022) 153001.

[5] I.C. Iakovides, K. Manoli, P. Karaolia, I. Michael-Kordatou, C.M. Manaia, D. Fatta-Kassinos, Reduction of antibiotic resistance determinants in urban wastewater by ozone: emphasis on the impact of wastewater matrix towards the inactivation kinetics, toxicity and bacterial regrowth, J. Hazard. Mater. 420 (2021), 126527, https://doi.org/10.1016/j.jhazmat.2021.126527.

[6] G. Reichert, S. Hilgert, J. Alexander, J.C. Rodrigues de Azevedo, T. Morck, S. Fuchs, T. Schwartz, Determination of antibiotic resistance genes in a WWTP-impacted river in surface water, sediment, and biofilm: influence of seasonality and water quality, Sci. Total Environ. 768 (2021), 144526, https://doi.org/10.1016/j.scitotenv.2020.144526.

[7] P. Karaolia, I. Michael-Kordatou, E. Hapeshi, C. Drosou, Y. Bertakis, D. Christofilos, G.S. Armatas, L. Sygellou, T. Schwartz, N.P. Xekoukoulotakis, D. Fatta-Kassinos, Removal of antibiotics, antibiotic-resistant bacteria and their associated genes by graphene-based TiO_2 composite photocatalysts under solar radiation in urban wastewaters, Appl. Catal. B Environ. 224 (2018) 810–824, https://doi.org/10.1016/j.apcatb.2017.11.020.

[8] N. Hembach, J. Alexander, C. Hiller, A. Wieland, T. Schwartz, Dissemination prevention of antibiotic resistant and facultative pathogenic bacteria by ultrafiltration and ozone treatment at an urban wastewater treatment plant, Sci. Rep. 9 (2019) 1–12, https://doi.org/10.1038/s41598-019-49263-1.

[9] M. Savin, J. Alexander, G. Bierbaum, J.A. Hammerl, N. Hembach, T. Schwartz, R. M. Schmithausen, E. Sib, A. Voigt, J. Kreyenschmidt, Antibiotic-resistant bacteria, antibiotic resistance genes, and antibiotic residues in wastewater from a poultry slaughterhouse after conventional and advanced treatments, Sci. Rep. 11 (2021) 1–11, https://doi.org/10.1038/s41598-021-96169-y.

[10] J. Alexander, G. Knopp, A. Dötsch, A. Wieland, T. Schwartz, Ozone treatment of conditioned wastewater selects antibiotic resistance genes, opportunistic bacteria, and induce strong population shifts, Sci. Total Environ. 559 (2016) 103–112, https://doi.org/10.1016/j.scitotenv.2016.03.154.

[11] A. Zarei-Baygi, A.L. Smith, Intracellular versus extracellular antibiotic resistance genes in the environment: prevalence, horizontal transfer, and mitigation strategies, Bioresour. Technol. 319 (2021) 124181, https://doi.org/10.1016/j.biortech.2020.124181.

[12] S. Li, C. Zhang, F. Li, T. Hua, Q. Zhou, S.H. Ho, Technologies towards antibiotic resistance genes (ARGs) removal from aquatic environment: a critical review, J. Hazard. Mater. 411 (2021) 125148, https://doi.org/10.1016/j.jhazmat.2021.125148.

[13] J. Alexander, A. Bollmann, W. Seitz, T. Schwartz, Microbiological characterization of aquatic microbiomes targeting taxonomical marker genes and antibiotic resistance genes of opportunistic bacteria, Sci. Total Environ. 512–513 (2015) 316–325, https://doi.org/10.1016/J.SCITOTENV.2015.01.046.

[14] N. Hembach, F. Schmid, J. Alexander, C. Hiller, E.T. Rogall, T. Schwartz, Occurrence of the mcr-1 colistin resistance gene and other clinically relevant antibiotic resistance genes in microbial populations at different municipal wastewater treatment plants in Germany, Front. Microbiol. 8 (2017) 1282, https://doi.org/10.3389/FMICB.2017.01282/BIBTEX.

[15] T. Ramamurthy, A. Ghosh, G.P. Pazhani, S. Shinoda, Current perspectives on viable but non-culturable (VBNC) pathogenic bacteria, Front. Public Heal. 2 (2014), https://doi.org/10.3389/FPUBH.2014.00103.

[16] S. Neubert, D. Mitoraj, S.A. Shevlin, P. Pulisova, M. Heimann, Y. Du, G.K.L. Goh, M. Pacia, K. Kruczała, S. Turner, W. MacYk, Z.X. Guo, R.K. Hocking, R. Beranek, Highly efficient rutile TiO_2 photocatalysts with single Cu(II) and Fe(III) surface catalytic sites, J. Mater. Chem. A. 4 (2016) 3127–3138, https://doi.org/10.1039/C5TA07036H.

[17] M. Endo, Z. Wei, K. Wang, B. Karabiyik, K. Yoshiiri, P. Rokicka, B. Ohtani, A. Markowska-Szczupak, E. Kowalska, Noble metal-modified titania with visible-light activity for the decomposition of microorganisms, Beilstein J. Nanotechnol. 9 (2018) 829–841, https://doi.org/10.3762/BJNANO.9.77.

[18] J.F. Gomes, K. Bednarczyk, M. Gmurek, M. Stelmachowski, A. Zaleska-Medynska, F.C. Bastos, M.E. Quinta-Ferreira, R. Costa, R.M. Quinta-Ferreira, R.C. Martins, Noble metal–TiO_2 supported catalysts for the catalytic ozonation of parabens mixtures, Process Saf. Environ. Prot. 111 (2017) 148–159.

[19] E. Borowska, J.F. Gomes, R.C. Martins, R.M. Quinta-Ferreira, H. Horn, M. Gmurek, Solar photocatalytic degradation of sulfamethoxazole by TiO_2 modified with noble metals, Catalysts 9 (2019) 500, https://doi.org/10.3390/catal9060500.

[20] E. Grabowska, M. Marchelek, T. Klimczuk, G. Trykowski, A. Zaleska-Medynska, Noble metal modified TiO_2 microspheres: surface properties and photocatalytic activity under UV–vis and visible light, J. Mol. Catal. A Chem. 423 (2016) 191–206, https://doi.org/10.1016/J.MOLCATA.2016.06.021.

[21] H. Gerischer, A. Heller, Photocatalytic oxidation of organic molecules at TiO_2 particles by sunlight in aerated water, J. Electrochem. Soc. 139 (1992) 113–118, https://doi.org/10.1149/1.2069154/XML.

[22] H. Gerischer, A. Heller, The role of oxygen in photooxidation of organic molecules on semiconductor particles, J. Phys. Chem. 95 (1991) 5261–5267, https://doi.org/10.1021/J100166A063/ASSET/J100166A063.FP.PNG_V03.

[23] N.F. Moreira, J.M. Sousa, G. Macedo, A.R. Ribeiro, L. Barreiros, M. Pedrosa, J. L. Faria, M.F.R. Pereira, S. Castro-Silva, M.A. Segundo, C.M. Manaia, O.C. Nunes, A.M.T. Silva, Photocatalytic ozonation of urban wastewater and surface water using immobilized TiO_2 with LEDs: Micropollutants, antibiotic resistance genes and estrogenic activity, Water Res. 94 (2016) 10–22, https://doi.org/10.1016/j.watres.2016.02.003.

[24] F. Baghal Asghari, M.H. Dehghani, R. Dehghanzadeh, D. Farajzadeh, D. Shanehbandi, A.H. Mahvi, K. Yaghmaeian, A. Rajabi, Performance evaluation of ozonation for removal of antibiotic-resistant Escherichia coli and Pseudomonas aeruginosa and genes from hospital wastewater, Sci. Rep. 11 (2021) 1–10, https://doi.org/10.1038/s41598-021-04254-z.

[25] L. Zhang, G. Meng, B. Liu, X. Ge, Heterogeneous photocatalytic ozonation of sulfamethoxazole by Z-scheme Bi_2WO_6/TiO_2 heterojunction: performance, mechanism and degradation pathway, J. Mol. Liq. 360 (2022) 119427.

[26] E. Asgari, M. Farzadkia, A. Esrafili, M.Y. Badi, S.F. Jokandan, H.R. Sobhi, Application of a photocatalytic ozonation process using TiO_2 magnetic nanoparticles for the removal of Ceftazide from aqueous solutions: Evaluation of performance, comparative study and mechanism, Optik (Stuttg) 212 (2020) 164667.

[27] V. Abromaitis, J. Svaikauskaite, A. Sulciute, D. Sinkeviciute, N. Zmuidzinaviciene, S. Misevicius, M. Tichonovas, I. Urniezaite, D. Jankunaite, M. Urbonavicius, S. Varnagiris, R. Dzingeleviciene, K. Baranauskis, D. Martuzevicius, Ozone-enhanced TiO_2 nanotube arrays for the removal of COVID-19 aided antibiotic ciprofloxacin from water: Process implications and toxicological evaluation, J. Environ. Manage. 318 (2022) 115515.

[28] A. Šuligoj, M. Kete, U. Černigoj, F. Fresno, U. Lavrenčič Štangar, Lavrenčič Štangar, Synergism in TiO_2 photocatalytic ozonation for the removal of dichloroacetic acid and thiacloprid, Environ. Res. 197 (2021) 110982.

[29] A.C. Mecha, M.N. Chollom, Photocatalytic ozonation of wastewater: a review, 18 (2020) 1491–1507. doi:10.1007/s10311-020-01020-x.

[30] Z. Pan, Q. Cai, Q. Luo, X. Li, Photocatalytic Ozonation of Oxalic Acid Over Cu(II)-Grafted TiO_2 Under Visible Light Irradiation, Http://Dx.Doi.Org/10.1080/15533174.2013.841207. 45 (2014) 447–450. doi:10.1080/15533174.2013.841207.

[31] Z. Wang, L. Zang, X. Fan, H. Jia, L. Li, W. Deng, C. Wang, Defect-mediated of Cu@TiO_2 core–shell nanoparticles with oxygen vacancies for photocatalytic degradation 2,4-DCP under visible light irradiation, Appl. Surf. Sci. 358 (2015) 479–484, https://doi.org/10.1016/J.APSUSC.2015.08.051.

[32] A. Payan, A. Akbar Isari, N. Gholizade, Catalytic decomposition of sulfamethazine antibiotic and pharmaceutical wastewater using Cu-TiO_2@functionalized SWCNT ternary porous nanocomposite: Influential factors, mechanism, and pathway studies, Chem. Eng. J. 361 (2019) 1121–1141, https://doi.org/10.1016/J.CEJ.2018.12.118.

[33] K.H. Leong, H.Y. Chu, S. Ibrahim, P. Saravanan, Palladium nanoparticles anchored to anatase TiO_2 for enhanced surface plasmon resonance-stimulated, visible-light-driven photocatalytic activity, Beilstein J. Nanotechnol. 643 (6) (2015) 428–437, https://doi.org/10.3762/BJNANO.6.43.

[34] M. Koohgard, M. Hosseini-Sarvari, Enhancement of Suzuki-Miyaura coupling reaction by photocatalytic palladium nanoparticles anchored to TiO_2 under visible

light irradiation, Catal. Commun. 111 (2018) 10–15, https://doi.org/10.1016/J.CATCOM.2018.03.026.

[35] B. Liu, B. Zhang, J. Ji, K. Li, J. Cao, Q. Feng, H. Huang, Effective regulation of surface bridging hydroxyls on TiO2 for superior photocatalytic activity via ozone treatment, Appl. Catal. B Environ. 304 (2022) 120952.

[36] T. Jäger, N. Hembach, C. Elpers, A. Wieland, J. Alexander, C. Hiller, G. Krauter, T. Schwartz, Reduction of antibiotic resistant bacteria during conventional and advanced wastewater treatment, and the disseminated loads released to the environment, Front. Microbiol. 9 (2018) 2599, https://doi.org/10.3389/FMICB.2018.02599/BIBTEX.

[37] A. Nocker, P. Sossa-Fernandez, M.D. Burr, A.K. Camper, Use of propidium monoazide for live/dead distinction in microbial ecology, Appl. Environ. Microbiol. 73 (16) (2007) 5111–5117.

[38] M. Miodyńska, A. Mikolajczyk, B. Bajorowicz, J. Zwara, T. Klimczuk, W. Lisowski, G. Trykowski, H.P. Pinto, A. Zaleska-Medynska, Urchin-like TiO2 structures decorated with lanthanide-doped Bi2S3 quantum dots to boost hydrogen photogeneration performance, Appl. Catal. B Environ. 272 (2020), 118962, https://doi.org/10.1016/J.APCATB.2020.118962.

[39] W.C. Peng, Y.C. Chen, J.L. He, S.L. Ou, R.H. Horng, D.S. Wuu, Tunability of p- and n-channel TiOx thin film transistors, Sci. Rep. 8 (2018), https://doi.org/10.1038/s41598-018-27598-5.

[40] V.V. Atuchin, V.G. Kesler, N.V. Pervukhina, Z. Zhang, Ti 2p and O 1s core levels and chemical bonding in titanium-bearing oxides, J. Electron Spectros. Relat. Phenomena 152 (2006) 18–24, https://doi.org/10.1016/J.ELSPEC.2006.02.004.

[41] N. Karikalan, R. Karthik, S.M. Chen, C. Karuppiah, A. Elangovan, Sonochemical synthesis of sulfur doped reduced graphene oxide supported CuS nanoparticles for the non-enzymatic glucose sensor applications, Sci. Rep. 7 (2017), https://doi.org/10.1038/s41598-017-02479-5.

[42] X. Wang, B. Zhang, W. Zhang, M. Yu, L. Cui, X. Cao, J. Liu, Super-light Cu@Ni nanowires/graphene oxide composites for significantly enhanced microwave absorption performance, Sci. Rep. 7 (2017), https://doi.org/10.1038/s41598-017-01529-2.

[43] M. Fronczak, A. Kasprzak, M. Bystrzejewski, Carbon-encapsulated iron nanoparticles with deposited Pd: a high-performance catalyst for hydrogenation of nitro compounds, J. Environ. Chem. Eng. 9 (1) (2021) 104673.

[44] M. Fronczak, E. Tálas, Z. Pászti, G.P. Szijjártó, J. Mihály, A. Tompos, P. Baranowski, S.K. Tiwari, M. Bystrzejewski, Photocatalytic performance of alkali metal doped graphitic carbon nitrides and Pd-alkali metal doped graphitic carbon nitride composites, Diam. Relat. Mater. 125 (2022), 109006, https://doi.org/10.1016/J.DIAMOND.2022.109006.

[45] S.S. El-Deen, A.M. Hashem, A.E. Abdel Ghany, S. Indris, H. Ehrenberg, A. Mauger, C.M. Julien, Anatase TiO2 nanoparticles for lithium-ion batteries, Ionics (Kiel) 24 (2018) 2925–2934, https://doi.org/10.1007/s11581-017-2425-y.

[46] F.D. Hardcastle, Raman spectroscopy of titania (TiO2) nanotubular water-splitting catalysts, J. Ark. Acad. Sci. 65 (2011) 43, https://doi.org/10.54119/jaas.2011.6504.

[47] J. Du, H. Sun, Polymer/TiO2 hybrid vesicles for excellent UV screening and effective encapsulation of antioxidant agents, ACS Appl. Mater. Interfaces 6 (2014) 13535–13541, https://doi.org/10.1021/am502663j.

[48] K. Sugiyama, Y. Takéuchi, The crystal structure of rutile as a function of temperature up to 1600°C, Zeitschrift Fur Krist. - New Cryst. Struct. 194 (1991) 305–313, https://doi.org/10.1524/ZKRI.1991.194.3-4.305/MACHINEREADABLECITATION/RIS.

[49] F. Zheng, Z. Wang, J. Chen, S. Li, Synthesis of carbon quantum dot-surface modified P25 nanocomposites for photocatalytic degradation of p-nitrophenol and acid violet 43, RSC Adv. 4 (2014) 30605–30609, https://doi.org/10.1039/c4ra02707h.

[50] H. Irie, S. Miura, K. Kamiya, K. Hashimoto, Efficient visible light-sensitive photocatalysts: Grafting Cu(II) ions onto TiO2 and WO3 photocatalysts, Chem. Phys. Lett. 457 (2008) 202–205, https://doi.org/10.1016/J.CPLETT.2008.04.006.

[51] G. Colón, Towards the hydrogen production by photocatalysis, Appl. Catal. A Gen. 518 (2016) 48–59, https://doi.org/10.1016/j.apcata.2015.11.042.

[52] L.F. Chiang, R. An Doong, Cu–TiO2 nanorods with enhanced ultraviolet- and visible-light photoactivity for bisphenol A degradation, J. Hazard. Mater. 277 (2014) 84–92, https://doi.org/10.1016/J.JHAZMAT.2014.01.047.

[53] O. Tahiri Alaoui, A. Herissan, C. Le Quoc, M.E.M. Zekri, S. Sorgues, H. Remita, C. Colbeau-Justin, Elaboration, charge-carrier lifetimes and activity of Pd-TiO2 photocatalysts obtained by gamma radiolysis, J. Photochem. Photobiol. A Chem. 242 (2012) 34–43, https://doi.org/10.1016/J.JPHOTOCHEM.2012.05.030.

[54] R. Camposeco, S. Castillo, I. Mejía-Centeno, J. Navarrete, J. Marín, Characterization of physicochemical properties of Pd/TiO2 nanostructured catalysts prepared by the photodeposition method, Mater. Charact. 95 (2014) 201–210, https://doi.org/10.1016/J.MATCHAR.2014.06.017.

[55] M.R. Espino-Estévez, C. Fernández-Rodríguez, O.M. González-Díaz, J. Araña, J. P. Espinós, J.A. Ortega-Méndez, J.M. Doña-Rodríguez, Effect of TiO2–Pd and TiO2–Ag on the photocatalytic oxidation of diclofenac, isoproturon and phenol, Chem. Eng. J. 298 (2016) 82–95, https://doi.org/10.1016/J.CEJ.2016.04.016.

[56] S. Sakthivel, M.V. Shankar, M. Palanichamy, B. Arabindoo, D.W. Bahnemann, V. Murugesan, Enhancement of photocatalytic activity by metal deposition: characterisation and photonic efficiency of Pt, Au and Pd deposited on TiO2 catalyst, Water Res. 38 (2004) 3001–3008, https://doi.org/10.1016/J.WATRES.2004.04.046.

[57] L. Kernazhitsky, V. Shymanovska, T. Gavrilko, V. Naumov, L. Fedorenko, V. Kshnyakin, J. Baran, Room temperature photoluminescence of anatase and rutile TiO2 powders, J. Lumin. 146 (2014) 199–204, https://doi.org/10.1016/j.jlumin.2013.09.068.

[58] M.R. Gillings, W.H. Gaze, A. Pruden, K. Smalla, J.M. Tiedje, Y.-G. Zhu, Using the class 1 integron-integrase gene as a proxy for anthropogenic pollution, ISME J. 9 (6) (2015) 1269–1279.

[59] M. Buchalska, M. Kobielusz, A. Matuszek, M. Pacia, S. Wojtyła, W. Macyk, On Oxygen Activation at Rutile- and Anatase-TiO2, ACS Catal. 5 (2015) 7424–7431, https://doi.org/10.1021/ACSCATAL.5B01562/ASSET/IMAGES/MEDIUM/CS-2015-01562T_0008.GIF.

[60] X. Huang, T. Li, X. Zhang, J. Deng, X. Yin, Bimetallic palladium@copper nanoparticles: lethal effect on the gram-negative bacterium Pseudomonas aeruginosa, Mater. Sci. Eng. C 129 (2021) 112392, https://doi.org/10.1016/J.MSEC.2021.112392.

[61] J. Nie, A.O.T. Patrocinio, S. Hamid, F. Sieland, J. Sann, S. Xia, D.W. Bahnemann, J. Schneider, New insights into the plasmonic enhancement for photocatalytic H2 production by Cu–TiO2 upon visible light illumination, Phys. Chem. Chem. Phys. 20 (2018) 5264–5273, https://doi.org/10.1039/C7CP07762A.

[62] E. Carrasco, J.C. Stockert, A. Juarranz, A. Blázquez-Castro, Plasmonic hot-electron reactive oxygen species generation: fundamentals for redox biology, Front. Chem. 8 (2020), https://doi.org/10.3389/fchem.2020.591325.

[63] E. Evgenidou, Z. Chatzisalata, A. Tsevis, K. Bourikas, P. Torounidou, D. Sergelidis, A. Koltsakidou, D.A. Lambropoulou, Photocatalytic degradation of a mixture of eight antibiotics using Cu-modified TiO2 photocatalysts: Kinetics, mineralization, antimicrobial activity elimination and disinfection, J. Environ. Chem. Eng. 9 (4) (2021) 105295.

[64] M.P. de la Flor, R. Camarillo, F. Martínez, C. Jiménez, R. Quiles, J. Rincón, Synthesis and characterization of bimetallic TiO2/CNT/Pd-Cu for efficient remediation of endocrine disruptors under solar light, J. Environ. Chem. Eng. 10 (2) (2022) 107245.

[65] K. Hoenes, R. Bauer, T. Meurle, B. Spellerberg, M. Hessling, Inactivation effect of violet and blue light on ESKAPE pathogens and closely related non-pathogenic bacterial species – A promising tool against antibiotic-sensitive and antibiotic-resistant microorganisms, Front. Microbiol. 11 (2021), 612367, https://doi.org/10.3389/fmicb.2020.612367.

[66] J.J. Alvear-Daza, J. Sanabria, J.A. Rengifo Herrera, H.M. Gutierrez-Zapata, Simultaneous abatement of organics (2,4-dichlorophenoxyacetic acid) and inactivation of resistant wild and laboratory bacteria strains by photo-induced processes in natural groundwater samples, Sol. Energy 171 (2018) 761–768, https://doi.org/10.1016/J.SOLENER.2018.07.026.

[67] Z. Yang, P. Liu, H. Wei, H. Li, J. Li, X. Qiu, R. Ding, X. Guo, Alteration in microbial community and antibiotic resistance genes mediated by microplastics during wastewater ultraviolet disinfection, Sci. Total Environ. 825 (2022) 153918.

[68] A. Zarei-Baygi, P. Wang, M. Harb, L.B. Stadler, A.L. Smith, Membrane fouling inversely impacts intracellular and extracellular antibiotic resistance gene abundances in the effluent of an anaerobic membrane bioreactor, cite this, Environ. Sci. Technol. 54 (2020) 12742–12751, https://doi.org/10.1021/acs.est.0c04787.

[69] I.C. Iakovides, I. Michael-Kordatou, N.F.F. Moreira, A.R. Ribeiro, T. Fernandes, M. F.R. Pereira, O.C. Nunes, C.M. Manaia, A.M.T. Silva, D. Fatta-Kassinos, Continuous ozonation of urban wastewater: removal of antibiotics, antibiotic-resistant Escherichia coli and antibiotic resistance genes and phytotoxicity, Water Res. 159 (2019) 333–347, https://doi.org/10.1016/J.WATRES.2019.05.025.

[70] J.M. Sousa, G. Macedo, M. Pedrosa, C. Becerra-Castro, S. Castro-Silva, M.F. R. Pereira, A.M.T. Silva, O.C. Nunes, C.M. Manaia, Ozonation and UV 254 nm radiation for the removal of microorganisms and antibiotic resistance genes from urban wastewater, J. Hazard. Mater. 323 (2017) 434–441.

[71] T. Matsunaga, R. Tomoda, T. Nakajima, H. Wake, Photoelectrochemical sterilization of microbial cells by semiconductor powders, FEMS Microbiol. Lett. 29 (1985) 211–214, https://doi.org/10.1111/j.1574-6968.1985.tb00864.x.

[72] Y. Deng, Z. Li, R. Tang, K. Ouyang, C. Liao, Y. Fang, C. Ding, L. Yang, L. Su, D. Gong, What will happen when microorganisms "meet" photocatalysts and photocatalysis? Environ. Sci. Nano 7 (2020) 702–723, https://doi.org/10.1039/c9en01318k.

[73] T.W. Ng, T. An, G. Li, W.K. Ho, H.Y. Yip, H. Zhao, P.K. Wong, The role and synergistic effect of the light irradiation and H2O2 in photocatalytic inactivation of Escherichia coli, J. Photochem. Photobiol. B Biol. 149 (2015) 164–171, https://doi.org/10.1016/j.jphotobiol.2015.04.007.

[74] S. Giannakis, A. Gupta, C. Pulgarin, J. Imlay, Identifying the mediators of intracellular E. coli inactivation under UVA light: the (photo) Fenton process and singlet oxygen, Water Res. 221 (2022), 118740, https://doi.org/10.1016/J.WATRES.2022.118740.